Advances in Applied Mathematics and Mechanics
Adv. Appl. Math. Mech., Vol. **17**, No. 1, pp. 31-68

DOI: 10.4208/aamm.OA-2022-0308
February 2025

An Improved WENO-Z+ Scheme

Ruo Li[1,2] and Wei Zhong[3,*]

[1] *CAPT, LMAM and School of Mathematical Sciences, Peking University, Beijing 100871, China*
[2] *Chongqing Research Institute of Big Data, Peking University, Chongqing 401121, China*
[3] *National Key Laboratory of Intense Pulsed Radiation Simulation and Effect, Northwest Institute of Nuclear Technology, Xi'an, Shaanxi 710024, China*

Received 24 November 2022; Accepted (in revised version) 18 May 2023

Abstract. The WENO-Z+ scheme [F. Acker, R. B. de R. Borges, and B. Costa, An improved WENO-Z scheme, J. Comput. Phys., 313 (2016), pp. 726–753] with two different versions further raised the nonlinear weights with respect to the nonsmooth or less-smooth substencils, by introducing an additional term into the weights formula of the well-validated WENO-Z scheme. These two WENO-Z+ schemes both produce less dissipative solutions than WENO-JS and WENO-Z. However, the recommended one which achieves superior resolutions in the high-frequency-wave regions fails to recover the designed order of accuracy where there exists a critical point, while the other one which obtains the designed order of accuracy at or near critical points is unstable near discontinuities. In the present study, we find that the WENO-Z+ schemes over-amplify the contributions from less-smooth substencils through their additional terms, and hence their improvements of both stability and resolution have been greatly hindered. Then, we develop improved WENO-Z+ schemes by making a set of modifications to the additional terms to avoid the over-amplification of the contributions from less-smooth substencils. The proposed schemes, denoted as WENO-IZ+, maintain the same convergence properties as the corresponding WENO-Z+ schemes. Numerical examples confirm that the new schemes are much more stable near discontinuities and far less dissipative in the region with high-frequency waves than the WENO-Z+ schemes. In addition, improved results have been obtained for one-dimensional linear advection problems, especially over long output times. The excellent performance of the new schemes is also demonstrated in the simulations of 1D and 2D Euler equation test cases.

AMS subject classifications: 65M06, 65M12

Key words: WENO scheme, high resolution, over-amplification, hyperbolic problems.

*Corresponding author.
Emails: rli@math.pku.edu.cn (R. Li), zhongwei2016@pku.edu.cn (W. Zhong)

1 Introduction

The first WENO (weighted essentially non-oscillatory) scheme was developed by Liu et al. [1] as an improvement to the ENO (essentially non-oscillatory) schemes [2–5]. Later, it was developed to recover the designed order of accuracy [6] resulting in the well-known WENO-JS scheme. Since this classical WENO-JS [6] scheme was proposed, the WENO schemes have been widely investigated [7–21, 48–51]. The WENO schemes owe their success to the ENO property near discontinuities and high-order accuracy in smooth regions.

It was pointed out by Henrick, Aslam and Powers [7] that WENO-JS may fail to obtain the designed order of accuracy at a point where the first derivative is zero while the second derivative is non-zero. To amend this drawback, they [7] devised the famous WENO-M scheme by constructing a mapping function to correct the classical WENO-JS weights. After that, a series of new mapping functions were designed leading to various versions of mapped WENO schemes [13–16,18–22]. As complicated mapping procedures are often required, the extra computational costs of most mapped WENO schemes are expensive.

Inspired by the work of Henrick et al. [7], Borges et al. [8] innovatively developed a very different way to determine the weights by incorporating the higher-order information about the numerical solution in the form of a global smoothness indicator (abbreviated to GSI). The new weights can satisfy the sufficient conditions for optimal convergence order, and thus, the new scheme, dubbed WENO-Z, recovers optimal convergence order even near critical points. Moreover, WENO-Z gains better results than WENO-M due to its lower dissipation while only consuming almost the same computational cost as that of the WENO-JS scheme. By designing different smoothness indicators or GSIs, a series of WENO-Z-type schemes [9–12, 23–26] were devised to further extend WENO-Z.

Compared to WENO-JS, WENO-M and WENO-Z both produce much less dissipation at or near critical points. And also, in high-frequency-wave regions, they both obtain greatly improved resolutions, especially for the standard shock-density wave interaction problems [27–30]. Since WENO-M and WENO-Z both show better convergence properties near the peak of the waves, the improved resolution of high-frequency waves was attributed to better accuracy at critical points. Until recently, it was revealed by Acker et al. [9] that assigning larger values to the nonlinear weights with respect to the nonsmooth or less-smooth substencils is the most relevant cause. Following this thought, Acker et al. [9] developed the improved WENO-Z scheme, dubbed WENO-Z+, by introducing an additional term into the weights formula of WENO-Z to further raise the nonlinear weights with respect to nonsmooth or less-smooth substencils. Two versions of WENO-Z+ were reported and both of them gained greatly better solutions compared to WENO-JS and WENO-Z on solving problems involving fine smooth structures and shocks [9]. However, increasing the nonlinear weights with respect to nonsmooth or less-smooth substencils also raises the potential risk of numerical instability. Therefore, the recommended version of WENO-Z+ enhances its stability at the price of violating the

optimality condition for the designed order of accuracy in the presence of critical points (see Proposition 6 of [9] for details). The other version of WENO-Z+ whose ϵ satisfies the optimality condition was more oscillatory than the recommended one, and as reported in [9], it generates evident spurious oscillations near discontinuities on simulating the Gaussian-square-triangle-ellipse test [6,9] and the shock-tube problem of Lax [31]. Actually, our calculations demonstrate that both of these two WENO-Z+ schemes, as well as the modified WENO-Z+ scheme (dubbed WENO-Z+I) proposed by Luo and Wu in [10], produce spurious oscillations in solving the standard shock-tube problem of Sod, albeit on a very small scale (see Fig. 10 in Subsection 5.2.1). And besides, the two versions of WENO-Z+ and WENO-Z+I really suffer from generating spurious oscillations or losing resolutions for long-output-time simulations of 1D linear advection equation with discontinuities (see Fig. 7 in Subsection 5.1.1) or high-order critical points (see Figs. 8, 9 in Subsection 5.1.2), as well as generating evident post-shock oscillations (see Figs. 21, 22, 23 in Subsection 5.3) for 2D Euler equations with strong shock waves. In this study, we try to reveal the reason why the WENO-Z+ schemes suffer from the troubles described above and to improve them accordingly.

The remainder of this article is structured under five major sections. First, in Section 2, we give a brief description of the finite-volume methodology and several different WENO schemes, including WENO-JS [6], WENO-Z [8], WENO-Z+ [9], as well as WENO-Z+I [10]. In Section 3, we discuss the over-amplification of the contributions from less-smooth substencils resulting from the additional term of WENO-Z+. The spectral properties of WENO-Z+ are also briefly provided in this section. The design of the improved WENO-Z+ schemes and the basic properties are proposed in Section 4. In Section 5, some numerical experiments are conducted to demonstrate the enhancements of the proposed schemes. Section 6 concludes this paper.

2 Preliminaries

In this section, we briefly describe several different fifth-order WENO schemes in the finite-volume framework for a clear understanding of the present work.

2.1 The finite-volume (FV) WENO method

This subsection focuses on the finite-volume (FV) WENO method. The FV method is a discretization method that is well-suited for the numerical simulation of hyperbolic conservation laws. For the convenience of description but without loss of generality, the following one-dimensional case is taken into account

$$\begin{cases} \dfrac{\partial u}{\partial t}+\dfrac{\partial f(u)}{\partial x}=0, \quad x_l\le x\le x_r, \quad t>0, \\ u(x,0)=u_0(x). \end{cases} \tag{2.1}$$

In the FV framework, a set of non-overlapping cells is used to discretize the computational domain. For simplicity, only the uniform mesh is discussed here. Let

$$\overline{u}_j(t)=\frac{1}{\Delta x}\int_{x_j-\Delta x/2}^{x_j+\Delta x/2}u(\xi,t)\mathrm{d}\xi,\quad \Delta x=x_{j+\frac{1}{2}}-x_{j-\frac{1}{2}}\quad\text{and}\quad I_j=[x_{j-\frac{1}{2}},x_{j+\frac{1}{2}}],$$

it is easy to know that $\overline{u}_j(t)$ indicates the volume-averaged conservative variable in I_j. In numerical calculations, our goal is to obtain an approximation to $\overline{u}_j(t)$.

By integrating the conservation law Eq. (2.1) over the cell I_j and after some simple mathematical manipulations, we can obtain

$$\frac{\mathrm{d}\bar{u}_j(t)}{\mathrm{d}t}\approx-\frac{1}{\Delta x}\left(\hat{f}_{j+\frac{1}{2}}-\hat{f}_{j-\frac{1}{2}}\right),\tag{2.2}$$

where $\overline{u}_j$ stands for the numerical approach to $\overline{u}_j(t)$. To compute $\hat{f}(u^-_{j\pm\frac{1}{2}},u^+_{j\pm\frac{1}{2}})$, some proper numerical fluxes are used. In this paper, we employ the Lax-Friedrichs (LF) flux [32, 33]. Once $u^\pm_{j\pm\frac{1}{2}}$ are calculated, the above ODE can be marched in time using a suitable time discretization method. In the present work, the widely used explicit, third-order, strong stability preserving (SSP) Runge–Kutta method [34–36] will be employed. WENO reconstructions are widely used to get $u^\pm_{j\pm\frac{1}{2}}$ and we next briefly review this to clarify our concerns. For the sake of brevity, we choose to only state the WENO procedures for $u^-_{j+\frac{1}{2}}$ and drop the superscript "$-$" without causing any confusion in the discussion below. It should be noted that $u^+_{j+\frac{1}{2}}$ can be reconstructed in a mirror-symmetric way.

2.2 Several WENO reconstructions

The 5th-order WENO reconstructions are defined as

$$u_{j+\frac{1}{2}}=\sum_{l=0}^{2}\omega_l u^l_{j+\frac{1}{2}},\tag{2.3}$$

where $u^l_{j+\frac{1}{2}}$, $l=0,1,2$ are the results of ENO [2–5] reconstructions with respect to three substencils, taking the form

$$u^0_{j+\frac{1}{2}}=\frac{1}{6}(2\bar{u}_{j-2}-7\bar{u}_{j-1}+11\bar{u}_j),\tag{2.4a}$$

$$u^1_{j+\frac{1}{2}}=\frac{1}{6}(-\bar{u}_{j-1}+5\bar{u}_j+2\bar{u}_{j+1}),\tag{2.4b}$$

$$u^2_{j+\frac{1}{2}}=\frac{1}{6}(2\bar{u}_j+5\bar{u}_{j+1}-\bar{u}_{j+2}).\tag{2.4c}$$

For WENO-JS [6], the nonlinear weights are given as

$$\omega_s^{\mathrm{JS}}=\frac{\alpha_s^{\mathrm{JS}}}{\sum_{l=0}^{2}\alpha_l^{\mathrm{JS}}},\quad \alpha_s^{\mathrm{JS}}=\frac{d_s}{(\beta_s+\epsilon)^p},\quad s=0,1,2,\tag{2.5}$$

where ϵ is a constant and very small positive real number introduced to prevent the denominator from becoming 0 (e.g., $\epsilon=10^{-40}$ is used in our numerical tests below), and $p=2$ is used usually. The smoothness indicators β_s are well defined in [6], and we can compute them by their explicit formulas as follows

$$\begin{aligned}
\beta_0&=\frac{13}{12}\left(\bar{u}_{j-2}-2\bar{u}_{j-1}+\bar{u}_j\right)^2+\frac{1}{4}\left(\bar{u}_{j-2}-4\bar{u}_{j-1}+3\bar{u}_j\right)^2,\\
\beta_1&=\frac{13}{12}\left(\bar{u}_{j-1}-2\bar{u}_j+\bar{u}_{j+1}\right)^2+\frac{1}{4}\left(\bar{u}_{j-1}-\bar{u}_{j+1}\right)^2,\\
\beta_2&=\frac{13}{12}\left(\bar{u}_j-2\bar{u}_{j+1}+\bar{u}_{j+2}\right)^2+\frac{1}{4}\left(3\bar{u}_j-4\bar{u}_{j+1}+\bar{u}_{j+2}\right)^2.
\end{aligned}$$

WENO-JS was found to dissipate too much and it was only third-order convergence order near critical points [7]. To fix this, WENO-Z was proposed [8] and its nonlinear weights are defined as

$$\omega_s^{\mathrm{Z}}=\frac{\alpha_s^{\mathrm{Z}}}{\sum_{l=0}^{2}\alpha_l^{\mathrm{Z}}},\quad \alpha_s^{\mathrm{Z}}=d_s\left[1+\left(\frac{\tau}{\beta_s+\epsilon}\right)^p\right], \tag{2.6}$$

where $\tau=|\beta_2-\beta_0|$. WENO-Z assigns larger weights to the less-smooth substencils than WENO-JS, leading to less-dissipative solutions. If taking $p=2$, WENO-Z can recover the fifth-order convergence rate of accuracy near critical points.

It was claimed that [9] the raising of the nonlinear weights with respect to nonsmooth or less-smooth substencils is the most relevant reason to elucidate the enhanced behavior of WENO-Z. Then, the following nonlinear weights were proposed

$$\omega_s^{\mathrm{Z+}}=\frac{\alpha_s^{\mathrm{Z+}}}{\sum_{l=0}^{2}\alpha_l^{\mathrm{Z+}}},\quad \alpha_s^{\mathrm{Z+}}=d_s\left[1+\left(\frac{\tau+\epsilon_\tau}{\beta_s+\epsilon_\beta}\right)^p+\zeta_s^{\mathrm{Z+}}\right],\quad \zeta_s^{\mathrm{Z+}}=\lambda\left(\frac{\beta_s+\epsilon_\beta}{\tau+\epsilon_\tau}\right), \tag{2.7}$$

in which an additional term was introduced into the weights formula of WENO-Z leading to the further raised nonlinear weights with respect to nonsmooth or less-smooth substencils.

Two different versions of WENO-Z+, dubbed WENO-Z+$^{\mathrm{A}}$ and WENO-Z+$^{\mathrm{B}}$ respectively in the present study, were reported in [9]. WENO-Z+$^{\mathrm{A}}$ stands for the version with the standard set of parameters, say, $\epsilon_\beta=\epsilon_\tau=10^{-40}$, $p=2$ and $\lambda=\Delta x^{2/3}$. WENO-Z+$^{\mathrm{B}}$ stands for the other version with the same parameters above, except for ϵ_β, which is changed to Δx^2. It was demonstrated that [9] WENO-Z+$^{\mathrm{A}}$ cannot obtain the designed order of accuracy in the presence of critical points and WENO-Z+$^{\mathrm{B}}$ achieves the designed order of accuracy, regardless of critical points. However, they also pointed out that WENO-Z+$^{\mathrm{B}}$ is more oscillatory than WENO-Z+$^{\mathrm{A}}$, and thus WENO-Z+$^{\mathrm{A}}$ was recommended in most applications [9].

Luo et al. [10] found that the improvement of WENO-Z+$^{\mathrm{A}}$ in solving problems with multiscale structures appeared to be insufficient compared to WENO-Z. To fix this issue,

they proposed some simple but efficient modifications to the nonlinear weights formula of WENO-Z+$^{\mathrm{A}}$, resulting in the following new weights formula

$$\omega_s^{\mathrm{Z+I}}=\frac{\alpha_s^{\mathrm{Z+I}}}{\sum_{l=0}^{2}\alpha_l^{\mathrm{Z+I}}}$$

with

$$\alpha_s^{\mathrm{Z+I}}=d_s\left[1+\left(\frac{\tau}{\beta_s+\epsilon}\right)^2+\lambda\left(1-\frac{\min(\beta_0,\beta_1,\beta_2)}{\max(\beta_0,\beta_1,\beta_2)+\epsilon^*}\right)\frac{\beta_s}{\max(\beta_0,\beta_1,\beta_2)+\epsilon}\right],$$

where $\epsilon^*=10^{-40}$ was taken in [10]. The other parameters are the same as those of WENO-Z+$^{\mathrm{A}}$, and the resultant scheme was named WENO-Z+I.

3 Analysis of the WENO-Z+ scheme

In this section, we review the WENO-Z+ scheme as introduced in subsection 2.2. We first discuss the risk of the appearance of spurious oscillations near discontinuities caused by the over-amplifications of the nonlinear weights with respect to the nonsmooth or less-smooth substencils resulting from the additional term. Then, we briefly present the spectral properties of WENO-Z+.

3.1 Over-amplifications of the nonlinear weights with respect to the nonsmooth or less-smooth substencils

It is well known that WENO-JS is too dissipative and raising the weights of less-smooth substencils leading to less-dissipative results, as WENO-Z+ does, seems to be beneficial to the solution in some cases. However, trivially, it is unfavorable to assign a larger weight to a less-smooth substencil while assigning a smaller weight to a smoother substencil as it may probably cause oscillations and instability. Therefore, the relative order of the nonlinear weights obtained from WENO-JS should be preserved. Otherwise, we say an over-amplification of the nonlinear weight with respect to a nonsmooth or less-smooth substencil happens. Unfortunately, WENO-Z+ can not prevent this over-amplification successfully. Here, we provide a brief analytical proof as follows, where the parameters ϵ, ϵ_τ, ϵ_β are dropped just for simplicity but without loss of generality.

Proposition 3.1. *Assume that $\mathcal{S}_{\mathrm{D}}$ is a substencil in which the solution is "less smooth" than that in $\mathcal{S}_{\mathrm{C}}$ which is a substencil of the same global stencil, in other words, $\beta_{\mathrm{D}}>\beta_{\mathrm{C}}$. If $\frac{d_{\mathrm{D}}}{d_{\mathrm{C}}}<\left(\frac{\beta_{\mathrm{D}}}{\beta_{\mathrm{C}}}\right)^p$, then we have*

(1). definitely, $\frac{\omega_{\mathrm{D}}^{\mathrm{JS}}}{\omega_{\mathrm{C}}^{\mathrm{JS}}}<1$;

(2). probably, $\frac{\omega_{\rm D}^{\rm Z+}}{\omega_{\rm C}^{\rm Z+}}>1$.

Proof. (1). Since $\frac{d_{\rm D}}{d_{\rm C}}<\left(\frac{\beta_{\rm D}}{\beta_{\rm C}}\right)^p$, according to Eq. (2.5), we have

$$\frac{\omega_{\rm D}^{\rm JS}}{\omega_{\rm C}^{\rm JS}}=\frac{\alpha_{\rm D}^{\rm JS}}{\alpha_{\rm C}^{\rm JS}}=\frac{d_{\rm D}/\beta_{\rm D}^p}{d_{\rm C}/\beta_{\rm C}^p}<1.$$

(2). Let

$$P_{\rm num}=d_{\rm D}\beta_{\rm C}^p\cdot\left(\beta_{\rm D}^p+\tau^p+\frac{\lambda\beta_{\rm D}^{p+1}}{\tau}\right)\quad\text{and}\quad P_{\rm den}=d_{\rm C}\beta_{\rm D}^p\cdot\left(\beta_{\rm C}^p+\tau^p+\frac{\lambda\beta_{\rm C}^{p+1}}{\tau}\right).$$

According to Eq. (2.7), we get

$$\frac{\omega_{\rm D}^{\rm Z+}}{\omega_{\rm C}^{\rm Z+}}=\frac{\alpha_{\rm D}^{\rm Z+}}{\alpha_{\rm C}^{\rm Z+}}=\frac{d_{\rm D}\beta_{\rm C}^p\cdot\left(\beta_{\rm D}^p+\tau^p+\lambda\beta_{\rm D}^{p+1}/\tau\right)}{d_{\rm C}\beta_{\rm D}^p\cdot\left(\beta_{\rm C}^p+\tau^p+\lambda\beta_{\rm C}^{p+1}/\tau\right)}=\frac{P_{\rm num}}{P_{\rm den}}=\frac{P_{\rm num}-P_{\rm den}}{P_{\rm den}}+1,\tag{3.1}$$

and

$$P_{\rm num}-P_{\rm den}=\underbrace{\beta_{\rm D}^p\beta_{\rm C}^p(d_{\rm D}-d_{\rm C})}_{T_1}+\underbrace{\tau^p\left(d_{\rm D}\beta_{\rm C}^p-d_{\rm C}\beta_{\rm D}^p\right)}_{T_2}+\underbrace{\frac{\lambda\beta_{\rm D}^p\beta_{\rm C}^p}{\tau}(d_{\rm D}\beta_{\rm D}-d_{\rm C}\beta_{\rm C})}_{T_3}.$$

Obviously, we have $T_2<0$ since $\frac{d_{\rm D}}{d_{\rm C}}<\left(\frac{\beta_{\rm D}}{\beta_{\rm C}}\right)^p$. For the case of $d_{\rm D}<d_{\rm C}$, if $\frac{d_{\rm D}}{d_{\rm C}}>\frac{\beta_{\rm C}}{\beta_{\rm D}}$, then we have $T_1<0$ and $T_3>0$. Therefore, we can not guarantee the inequality of $P_{\rm num}-P_{\rm den}<0$. In other words, the inequality $P_{\rm num}-P_{\rm den}>0$ may hold, leading to $\frac{\omega_{\rm D}^{\rm Z+}}{\omega_{\rm C}^{\rm Z+}}>1$. For the case of $d_{\rm D}>d_{\rm C}$, it is trivial to get $T_1>0$ and $T_3>0$. Similarly, we probably have $\frac{\omega_{\rm D}^{\rm Z+}}{\omega_{\rm C}^{\rm Z+}}>1$. Actually, we can directly verify the second case from the last two rows of Table 1 in [9]. □

To manifest Proposition 3.1 and illustrate the negative effect of the over-amplifications of the nonlinear weights with respect to the nonsmooth or less-smooth substencils, we consider the following model test proposed in [9]

$$F(x)=\frac{2}{3}\sin(6\pi x)+\frac{1}{4}\sin(1.6\pi x).\tag{3.2}$$

Now we examine the behavior of WENO-Z+$^{\rm A}$ and WENO-Z+$^{\rm B}$ with $\Delta x=1/20$. For the purpose of comparison, we illustrate the solutions solved by WENO-Z+$^{\rm A}$ (Fig. 1(a)) and WENO-Z+$^{\rm B}$ (Fig. 1(b)) and their nonlinear weights, as well as that of WENO-JS, together in Fig. 1. The X-axis is x, the left Y-axis is $F(x)$, and the right Y-axis is the nonlinear

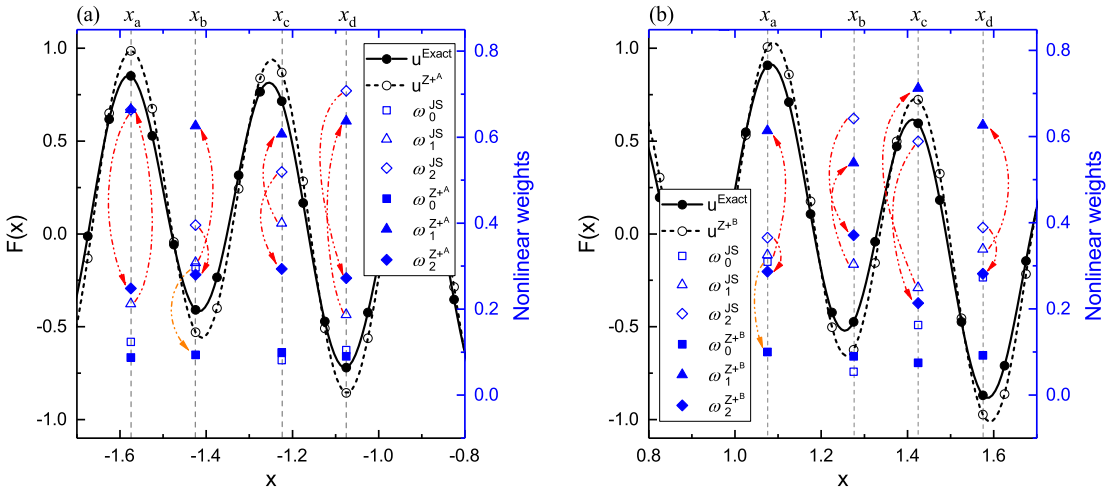

Figure 1: Left axis (in black): the numerical solutions and the exact solution of $F(x)$ with $\Delta x=1/20$. Right axis (in blue): the nonlinear weights of different WENO schemes. The double dot-dash arrow lines (in red) illustrate the over-amplifications of the nonlinear weights with respect to the nonsmooth or less-smooth substencils.

weights. Firstly, we can see that, at x_b of Fig. 1(a) and x_a of Fig. 1(b), $\omega_0^{\rm JS}$ is very close to $\omega_1^{\rm JS}$, while $\omega_0^{\rm Z+^A}$ and $\omega_0^{\rm Z+^B}$ are far smaller than $\omega_1^{\rm Z+^A}$ and $\omega_1^{\rm Z+^B}$ respectively. Moreover, it can be seen that both WENO-Z+$^{\rm A}$ and WENO-Z+$^{\rm B}$ over-amplify the contributions from less-smooth substencils near critical points. In other words, Proposition 3.1 holds at these locations leading to the fact that a larger weight is assigned to a less-smooth substencil while a smaller weight is assigned to a smoother substencil. Accordingly, we find that the computed results of $F(x)$ near these critical points are significantly larger than the exact solution. It is well known that [9,13] it is difficult to distinguish discontinuities from high gradients and fine smooth structures by the smoothness indicators. Therefore, the results above and Proposition 3.1 indicate that WENO-Z+$^{\rm A}$ and WENO-Z+$^{\rm B}$ may fail to maintain the ENO property near discontinuities resulting in spurious oscillations and instability. Actually, it was shown in Fig. 22 of [9] that WENO-Z+$^{\rm B}$, which satisfies Proposition 6 of [9] leading to optimal convergence orders even near critical points, generates evident spurious oscillations. Therefore, to better avoid spurious oscillations, WENO-Z+$^{\rm A}$ was recommended by [9] although its convergence rate of accuracy near critical points is only third order. Furthermore, our calculations as given in Fig. 10 below demonstrate that both WENO-Z+$^{\rm A}$ and WENO-Z+$^{\rm B}$ produce spurious oscillations near discontinuities.

Besides causing instability, the over-amplifications of the nonlinear weights with respect to the nonsmooth or less-smooth substencils may also hinder the improvement of the resolution of WENO-Z+$^{\rm A}$ and WENO-Z+$^{\rm B}$, especially for long-run simulations (see Figs. 7, 8, 9 below) and for problems with severe high-frequency smooth waves (see Figs. 14, 15, 20 below). We will discuss this carefully in Section 5.

3.2 The spectral analysis

By using the approximated dispersion relation (ADR) method proposed by Pirozzoli [37], the spectral properties of WENO-Z+$^{\mathrm{A}}$ was investigated carefully by Luo et al. in [10] in which special attention has been paid to the dissipation property of WENO-Z+$^{\mathrm{A}}$. It was indicated that the additional term of WENO-Z+$^{\mathrm{A}}$, say, $\lambda\left(\frac{\beta_s+\epsilon_\beta}{\tau_5+\epsilon_\tau}\right)$, may cause negative dissipation, that is, the imaginary part of the modified wavenumbers is positive. Although the negative-dissipation interval can be narrowed down by decreasing the value of λ, there is a singularity located at the wavenumber of $\varphi\approx 1.18$ that can not be eliminated even if λ has been reduced to the recommended value of $\Delta x^{2/3}$. Luo et al. [10] concluded that this singularity is harmful to the resolution of WENO-Z+$^{\mathrm{A}}$ and one can refer to [10] for a detailed analysis. In summary, it is necessary to eliminate this singularity in the design of the improved WENO-Z+$^{\mathrm{A}}$, as well as WENO-Z+$^{\mathrm{B}}$. In subsection 4.3 below, we will discuss this in detail.

4 Design and properties of the improved WENO-Z+ scheme

4.1 The new nonlinear weights

Inspired by the knowledge discussed earlier, we propose a means of improving the family of WENO-Z+ schemes, by preventing the over-amplifications of the nonlinear weights with respect to the nonsmooth or less-smooth substencils. The idea is to modify the additional term of $\alpha_s^{\mathrm{Z}+}$, resulting in the formula

$$\alpha_s^{\mathrm{IZ}+}=d_s\left(1+\left(\frac{\tau+\epsilon_\tau}{\beta_s+\epsilon_\beta}\right)^p+\zeta_s^*\right). \tag{4.1}$$

In the regions where no over-amplification happens, the modified additional term ζ_s^* should satisfy the same conditions as that $\zeta_s^{\mathrm{Z}+}$ satisfies stated on page 734 of [9]. But, in the regions where over-amplification happens, the modified term ζ_s^* should help to eliminate the over-amplification, and a simple way to do this is to turn $\alpha_s^{\mathrm{IZ}+}$ back into that of WENO-JS, say, α_s^{JS}. Directed by this idea, we devise such a ζ_s^* as follows

$$\zeta_s^*=\theta\zeta_s^{\mathrm{Z}+}+\frac{1-\theta}{(\beta_s+\epsilon_\beta)^p}\left(1-(\beta_s+\epsilon_\beta)^p-(\tau+\epsilon_\tau)^p\right), \tag{4.2}$$

with

$$\theta=\begin{cases}1, & \text{if } \min\limits_{\substack{0\le i,j\le 2\\ i\neq j}}\Theta(i,j)>0,\\ 0, & \text{otherwise,}\end{cases} \tag{4.3}$$

where

$$\Theta(i,j)=\left(\frac{\alpha_i^{\mathrm{JS}}}{\alpha_j^{\mathrm{JS}}+\epsilon}-1\right)\left(\frac{\alpha_i^{\mathrm{Z}+}}{\alpha_j^{\mathrm{Z}+}+\epsilon}-1\right)$$

is used to detect the over-amplification of the nonlinear weights with respect to the non-smooth or less-smooth substencils, and we trivially have the following property.

Proposition 4.1. *If for $\forall i,j=0,1,2$ and $i\neq j$, $\Theta(i,j)>0$ holds true, then we say there is no over-amplifications of the nonlinear weights with respect to the nonsmooth or less-smooth substencils on the corresponding set of substencils for WENO-Z+. Otherwise, the over-amplification happens.*

Therefore, we obtain the improved nonlinear weights formula as follows

$$\omega_s^{\mathrm{IZ}+}=\frac{\alpha_s^{\mathrm{IZ}+}}{\sum_{l=0}^{2}\alpha_l^{\mathrm{IZ}+}}, \tag{4.4}$$

where $\alpha_s^{\mathrm{IZ}+}$ is computed by Eqs. (4.1), (4.2) and (4.3). We denote this improved WENO-Z+ scheme as WENO-IZ+. Specifically, for the case of $\epsilon_\tau=\epsilon_\beta=10^{-40}$, $p=2$ and $\lambda=\Delta x^{2/3}$, WENO-IZ+$^{\mathrm{A}}$ and $\omega_s^{\mathrm{IZ}+^{\mathrm{A}}}$ are used. Similarly, WENO-IZ+$^{\mathrm{B}}$ and $\omega_s^{\mathrm{IZ}+^{\mathrm{B}}}$ are used for the case that ϵ_β is changed to Δx^2 while the other parameters are the same as those of WENO-IZ+$^{\mathrm{A}}$, so as to achieve the designed orders of accuracy regardless of critical points.

Now, in comparison to Proposition 3.1, we give the following Proposition 4.2 for the WENO-IZ+ schemes.

Proposition 4.2. *Assume that $\mathcal{S}_{\mathrm{D}}$ is a substencil in which the solution is "less smooth" than that in $\mathcal{S}_{\mathrm{C}}$ which is a substencil of the same global stencil, in other words, $\beta_{\mathrm{D}}>\beta_{\mathrm{C}}$. If $\frac{d_{\mathrm{D}}}{d_{\mathrm{C}}}<\left(\frac{\beta_{\mathrm{D}}}{\beta_{\mathrm{C}}}\right)^p$, then we definitely have*

$$\frac{\omega_{\mathrm{D}}^{\mathrm{JS}}}{\omega_{\mathrm{C}}^{\mathrm{JS}}}\leq\frac{\omega_{\mathrm{D}}^{\mathrm{IZ}+}}{\omega_{\mathrm{C}}^{\mathrm{IZ}+}}<1.$$

Proof. The proof of $\frac{\omega_{\mathrm{D}}^{\mathrm{JS}}}{\omega_{\mathrm{C}}^{\mathrm{JS}}}<1$ is exactly the same as that of Proposition 3.1.

(1). If

$$\min_{\substack{0\leq i,j\leq 2\\ i\neq j}}\Theta(i,j)>0$$

as $\frac{\omega_{\mathrm{D}}^{\mathrm{JS}}}{\omega_{\mathrm{C}}^{\mathrm{JS}}}<1$, we can trivially know that $\frac{\alpha_{\mathrm{D}}^{\mathrm{Z}+}}{\alpha_{\mathrm{C}}^{\mathrm{Z}+}}-1<0$ (disregarding ϵ), leading to $\frac{\omega_{\mathrm{D}}^{\mathrm{Z}+}}{\omega_{\mathrm{C}}^{\mathrm{Z}+}}<1$. From Eq. (4.3), we obtain $\theta=1$, then we get $\zeta_s^*=\zeta_s^{\mathrm{Z}+}$ according to Eq. (4.2). Thus, $\omega_s^{\mathrm{IZ}+}$ is equal to $\omega_s^{\mathrm{Z}+}$. So, we have $\frac{\omega_{\mathrm{D}}^{\mathrm{IZ}+}}{\omega_{\mathrm{C}}^{\mathrm{IZ}+}}<1$, and clearly,

$$\frac{\omega_{\mathrm{D}}^{\mathrm{IZ}+}}{\omega_{\mathrm{C}}^{\mathrm{IZ}+}}=\frac{\omega_{\mathrm{D}}^{\mathrm{Z}+}}{\omega_{\mathrm{C}}^{\mathrm{Z}+}}=\frac{\alpha_{\mathrm{D}}^{\mathrm{Z}+}}{\alpha_{\mathrm{C}}^{\mathrm{Z}+}}=\frac{d_{\mathrm{D}}\beta_{\mathrm{C}}^p\cdot\left(\beta_{\mathrm{D}}^p+\tau^p+\lambda\beta_{\mathrm{D}}^{p+1}/\tau\right)}{d_{\mathrm{C}}\beta_{\mathrm{D}}^p\cdot\left(\beta_{\mathrm{C}}^p+\tau^p+\lambda\beta_{\mathrm{C}}^{p+1}/\tau\right)}>\frac{d_{\mathrm{D}}/\beta_{\mathrm{D}}^p}{d_{\mathrm{C}}/\beta_{\mathrm{C}}^p}=\frac{\omega_{\mathrm{D}}^{\mathrm{JS}}}{\omega_{\mathrm{C}}^{\mathrm{JS}}}.$$

(2). Otherwise, we have $\theta=0$. Then, it is very easy to verify that $\alpha_s^{\mathrm{IZ}+}=\alpha_s^{\mathrm{JS}}$. In other words, we have

$$\frac{\omega_{\mathrm{D}}^{\mathrm{IZ}+}}{\omega_{\mathrm{C}}^{\mathrm{IZ}+}}=\frac{\omega_{\mathrm{D}}^{\mathrm{JS}}}{\omega_{\mathrm{C}}^{\mathrm{JS}}}.$$

Thus, we complete the proof. □

Clearly, the convergence property of WENO-IZ+ is identical to that of the corresponding WENO-Z+ which has been discussed carefully in [9]. In other words, WENO-IZ+$^{\mathrm{A}}$ can achieve only 3rd-order accuracy where there is a first-order critical point while WENO-IZ+$^{\mathrm{B}}$ can recover the designed convergence orders. In Section 4.4 below, we will numerically verify this in detail.

4.2 Verification and demonstration

Now, we verify the fact that WENO-IZ+$^{\mathrm{A}}$ and WENO-IZ+$^{\mathrm{B}}$ can successfully eliminate the over-amplifications of the nonlinear weights with respect to the nonsmooth or less-smooth substencils, by considering the model test Eq. (3.2) used earlier. And also, we will roughly demonstrate the benefit of the new schemes through this test.

Similarly, we plot the results computed by WENO-IZ+$^{\mathrm{A}}$ (left figure) and WENO-IZ+$^{\mathrm{B}}$ (right figure) and the nonlinear weights of WENO-JS and WENO-IZ+$^{\mathrm{A}}$ or WENO-IZ+$^{\mathrm{B}}$ together in Fig. 2. Again, the X-axis is x, the left Y-axis is $F(x)$, and the right Y-axis is the nonlinear weights. We can see that the over-amplifications of the nonlinear weights with respect to the nonsmooth or less-smooth substencils generated by WENO-Z+$^{\mathrm{A}}$ and WENO-Z+$^{\mathrm{B}}$ as shown in Fig. 1 have been successfully eliminated by WENO-IZ+$^{\mathrm{A}}$ and WENO-IZ+$^{\mathrm{B}}$. As a result, it can be found that the corresponding computed results of $F(x)$ are properly bounded by the exact solution. This is a remarkable benefit of the new schemes as it indicates that WENO-IZ+$^{\mathrm{A}}$ and WENO-IZ+$^{\mathrm{B}}$ are more stable than the corresponding WENO-Z+$^{\mathrm{A}}$ and WENO-Z+$^{\mathrm{B}}$. We will examine this carefully through

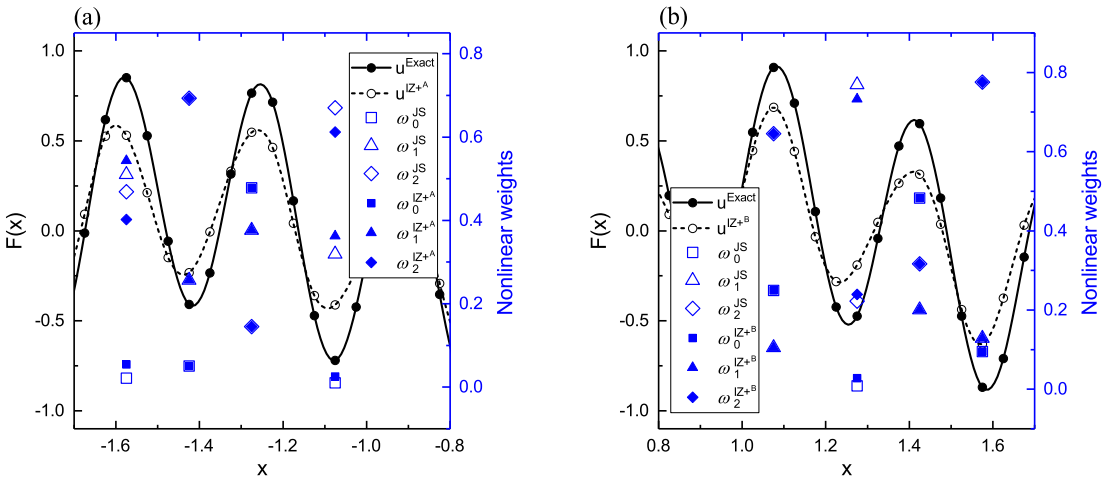

Figure 2: Left axis (in black): the numerical solutions solved by WENO-IZ+$^{\mathrm{A}}$, WENO-IZ+$^{\mathrm{B}}$ and the exact solution of $F(x)$ with $\Delta x = 1/20$. Right axis (in blue): nonlinear weights of WENO-IZ+$^{\mathrm{A}}$, WENO-IZ+$^{\mathrm{B}}$ and WENO-JS. For comparison with Fig. 1.

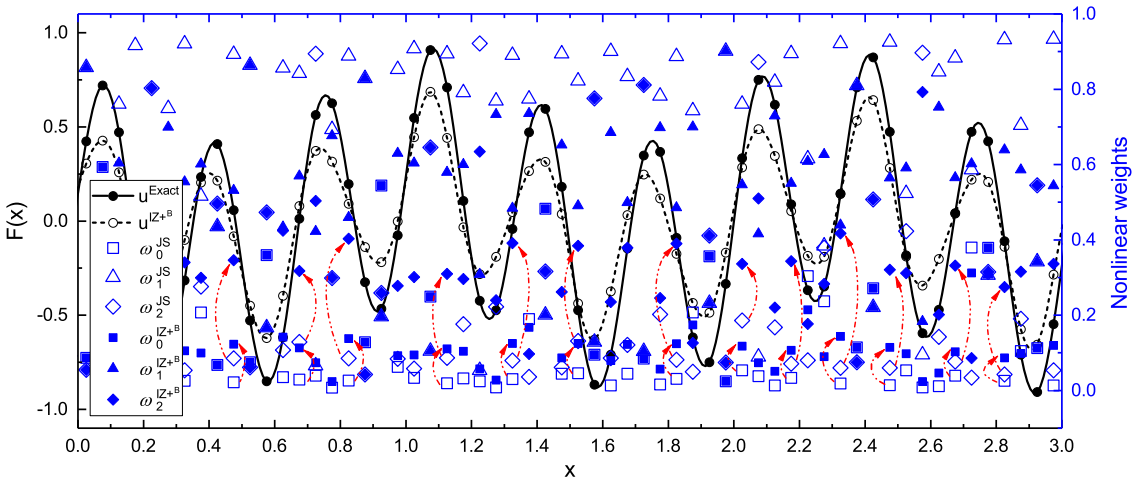

Figure 3: Left axis (in black): the numerical solution solved by WENO-IZ+$^{\mathrm{B}}$ and the exact solution of $F(x)$ with $\Delta x=1/20$. Right axis (in blue): nonlinear weights of WENO-IZ+$^{\mathrm{B}}$ and WENO-JS. To show more results. The dashed arrow lines (in red) illustrate the increase of the weights of less-smooth substencils.

numerical experiments in Section 5.

It is worth noting that there are still many locations where the weights of less-smooth substencils are increased by WENO-IZ+$^{\mathrm{A}}$ and WENO-IZ+$^{\mathrm{B}}$, and we can see this clearly in Fig. 3 where more results of WENO-IZ+$^{\mathrm{B}}$ are plotted as an illustrative example. This means that WENO-IZ+$^{\mathrm{B}}$, as well as WENO-IZ+$^{\mathrm{A}}$ whose results are similar to that of WENO-IZ+$^{\mathrm{B}}$ while not presented here just for the sake of brevity, maintains the major feature of WENO-Z+ of increasing the weights of less-smooth substencils at most locations, which was claimed [9] to be beneficial to the solution for some cases.

4.3 Dispersion and dissipation properties

In this subsection, we investigate the spectral properties of the WENO-IZ+$^{\mathrm{A}}$ and WENO-IZ+$^{\mathrm{B}}$ schemes. For nonlinear WENO schemes, the spectral properties can be obtained by using the approximated dispersion relation (ADR) method proposed by Pirozzoli [37]. The ADR of a nonlinear scheme is obtained by numerically advancing sinusoidal test functions with reduced wavenumber, say φ, up to a very short time τ, and determining the resulting wave amplitude through Fourier transform, say $\hat{v}(\varphi;\tau)$. On a finite uniform mesh with length L and N mesh cells, the supported Fourier modes have wavelengths $\lambda_n=L/n$ and reduced wavenumbers $\varphi_n=2\pi n/(N-1)$, $0\leq\varphi_n\leq\pi$ with $n=0,\cdots,(N-1)/2$. Then, a discrete representation of the spectral transfer function can be obtained by

$$\Phi(\varphi_n)=-\frac{1}{\mathrm{i}\sigma}\log\left(\frac{\hat{v}(\varphi_n;\tau)}{\hat{v}_0(\varphi_n)}\right),\quad n=0,\cdots,N/2,$$

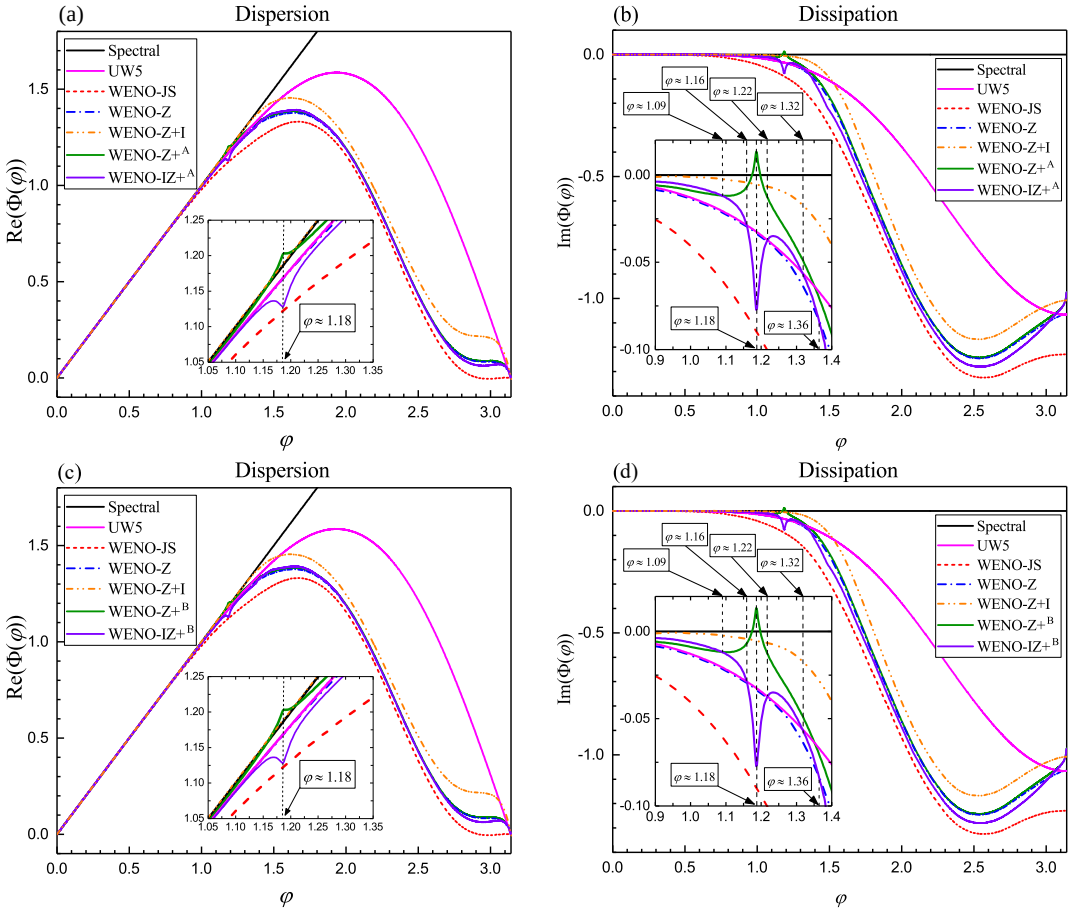

Figure 4: Comparison of the dispersion and dissipation properties of different schemes.

where $\sigma = c\tau/\Delta x \ll 1$. It is indicated that [37] the real part of Φ is associated with the approximate phase speed, i.e., with the dispersion properties of the scheme, while the imaginary part of Φ is related to its numerical dissipation.

For comparison purposes, Fig. 4 gives the spectral properties of the WENO-IZ+^{A}, WENO-IZ+^{B} schemes and their associated WENO-Z+^{A}, WENO-Z+^{B} schemes, as well as the fifth-order upwind (UW5) scheme and the classical WENO-JS and WENO-Z schemes. In general, WENO-IZ+^{A} and WENO-IZ+^{B} gain almost the same dispersion and dissipation properties, outperforming those of WENO-JS.

Now, let us focus our discussion on the dissipation property of the schemes shown in Fig. 4. We can observe that: (1) firstly, it is consistent with the results proposed in [10] that WENO-Z+^{A}, as well as WENO-Z+^{B}, embraces a singularity at about $\varphi = 1.18$ around where the negative dissipation occurs; (2) however, this negative-dissipation interval is eliminated by WENO-IZ+^{A} and WENO-IZ+^{B}; (3) in the region of low modified

wavenumbers of $\varphi<1.09$, the dissipation of WENO-IZ+$^{\mathrm{A}}$ and WENO-IZ+$^{\mathrm{B}}$ is slightly smaller than that of WENO-Z+$^{\mathrm{A}}$ and WENO-Z+$^{\mathrm{B}}$; (4) in the region of low and medium modified wavenumbers of $\varphi<1.36$ excluding the interval of $\varphi\in(1.16,1.22)$ around the singularity, WENO-IZ+$^{\mathrm{A}}$ and WENO-IZ+$^{\mathrm{B}}$ show smaller dissipation than WENO-Z; (5) moreover, the dissipation of WENO-IZ+$^{\mathrm{A}}$ and WENO-IZ+$^{\mathrm{B}}$ is even smaller than that of the UW5 scheme in the region of low and medium modified wavenumbers of $\varphi<1.32$ excluding the interval of $\varphi\in(1.16,1.22)$. It should be pointed out that the dissipation property of the ADR of WENO-IZ+$^{\mathrm{A}}$ is inferior to those of WENO-Z+$^{\mathrm{A}}$, WENO-Z and WENO-Z+I in the region of medium and high wavenumbers. However, for the long-run solutions with discontinuities (for example, see Fig. 7 below) and high-order critical points in smooth regions (for example, see Fig. 8 and Fig. 9 below), WENO-IZ+$^{\mathrm{A}}$ is much less dissipative than WENO-Z+$^{\mathrm{A}}$, WENO-Z and WENO-Z+I, and as pointed out by Zeng et al. [26], this fact demonstrates that the anti-dissipation of WENO-IZ$^{\mathrm{A}}$ is effective for both smooth solution and discontinuous solution, while WENO-Z+$^{\mathrm{A}}$, WENO-Z and WENO-Z+I can only improve the accuracy of the smooth solution, especially for long output time simulations. Besides WENO-IZ+$^{\mathrm{A}}$, the dissipation property of WENO-IZ+$^{\mathrm{B}}$ is also inferior to those of WENO-Z+$^{\mathrm{B}}$, WENO-Z and WENO-Z+I in the region of medium and high wavenumbers. Similarly, WENO-IZ+$^{\mathrm{B}}$ is much less dissipative than WENO-Z and WENO-Z+I, especially for long-run calculations. Although the dissipation of WENO-Z+$^{\mathrm{B}}$ is as small as WENO-IZ+$^{\mathrm{B}}$, it is far less robust than WENO-IZ+$^{\mathrm{B}}$ (see Figs. 5, 6, 7 of Subsection 5.1 and Figs. 10, 11 of Subsection 5.2). This fact demonstrates that the anti-dissipation of WENO-IZ+$^{\mathrm{B}}$ is helpful to avoid spurious oscillations for the discontinuous solutions, while WENO-Z+$^{\mathrm{B}}$ can not prevent spurious oscillations near discontinuities.

4.4 Convergence property at smooth critical points

In this subsection, we conduct a numerical test to examine the convergence property of the WENO-IZ+$^{\mathrm{A}}$ and WENO-IZ+$^{\mathrm{B}}$ schemes at smooth critical points.

Consider the following classical test case

$$g(x)=x^n\mathrm{e}^x,\quad -1.0\le x\le 1.0.$$

It is very easy to verify that its first $n-1$ derivatives $g^{(j)}(x_{\mathrm{cp}})=0$, $j=0,1,\cdots,n-1$ with $x_{\mathrm{cp}}=0$. In other words, the function $g(x)$ has a $(n-1)$st-order critical point at x_{cp}.

Taking $n=2$, the L_∞ convergence properties are shown in Table 1. As expected, the convergence order of the WENO-JS scheme drops to about third-order, and the WENO-Z and WENO-Z+I schemes can recover the optimal convergence order. In consistency with the results given in [9], WENO-Z+$^{\mathrm{A}}$ also only obtains nearly 3rd-order convergence order of accuracy while the WENO-Z+$^{\mathrm{B}}$ scheme achieves the 5th-order convergence order of accuracy, leading to the fact that their improved WENO-IZ+$^{\mathrm{A}}$ and WENO-IZ+$^{\mathrm{B}}$ schemes get third-order and fifth-order accuracy respectively. In terms of accuracy, the WENO-Z, WENO-Z+I, WENO-Z+$^{\mathrm{B}}$ and WENO-IZ+$^{\mathrm{B}}$ schemes significantly outperform

Table 1: Convergence properties at the smooth critical point.

N	100	200	400	800	1600	3200
WENO-JS	7.78472E-06	8.25085E-07	8.74036E-08	9.20947E-09	9.65225E-10	1.00658E-10
	-	3.2380	3.2388	3.2465	3.2542	3.2614
WENO-Z	8.51117E-08	1.58511E-09	3.75866E-11	8.72344E-13	1.99977E-14	4.54841E-16
	-	5.7467	5.3982	5.4292	5.4470	5.4583
WENO-Z+I	6.24936E-08	8.67724E-10	1.53728E-11	1.94040E-13	5.27482E-15	1.62034E-16
	-	6.1703	5.8188	6.3079	5.2011	5.0248
WENO-Z+^{A}	1.88414E-06	2.41769E-07	2.90637E-08	3.37702E-09	3.81995E-10	4.22559E-11
	-	2.9622	3.0563	3.1054	3.1441	3.1763
WENO-IZ+^{A}	1.88363E-06	2.41769E-07	2.90637E-08	3.37702E-09	3.81995E-10	4.22559E-11
	-	2.9618	3.0563	3.1054	3.1441	3.1763
WENO-Z+^{B}	2.19534E-08	7.17315E-10	2.24974E-11	7.03379E-13	2.19788E-14	6.86759E-16
	-	4.9357	4.9948	4.9993	5.0001	5.0002
WENO-IZ+^{B}	1.55846E-08	7.17316E-10	2.24974E-11	7.03379E-13	2.19788E-14	6.86759E-16
	-	4.4414	4.9948	4.9993	5.0001	5.0002

the WENO-JS, WENO-Z+^{A} and WENO-IZ+^{A} schemes. Furthermore, we can see that the numerical errors and convergence orders of the WENO-IZ+^{A} and WENO-IZ+^{B} schemes are identical to those of their counterparts, say, WENO-Z+^{A} and WENO-Z+^{B}, respectively.

5 Numerical results

In this section, we compare the numerical performance of WENO-IZ+^{A} and WENO-IZ+^{B} with WENO-Z+^{A} and WENO-Z+^{B}, as well as the classical WENO-JS and WENO-Z. And also, the solution of WENO-Z+I is provided. The numerical presentation starts with two different cases of the 1D scalar advection equation. One is discontinuous to demonstrate the excellent robustness and high-resolution property of the proposed WENO-IZ+^{A} and WENO-IZ+^{B} dealing with complicated cases, and the other is smooth with high-order critical points to demonstrate that these new schemes can provide considerably high-resolution results for simulations with large output times while the other considered schemes do not. Then, the one-dimensional Euler equations with Riemann initial value problems of Sod and Lax, shock-density wave interaction of Shu-Osher and Titarev-Toro and the interacting blast problems are conducted to further demonstrate the strong robustness and high-resolution property of the proposed schemes. Finally, the two-dimensional problems on the 2D version of the shock-density wave interaction, shock-vortex interaction, two-dimensional Riemann problem, Rayleigh-Taylor instability and double Mach reflection are simulated. Unless noted otherwise, the CFL number is set to be 0.5 for all calculations.

5.1 1D scalar advection equation

1D scalar advection equation is defined by

$$\begin{cases} u_t+u_x=0, & -1\le x\le 1,\\ u(x,0)=u_0(x), & \text{periodic boundary.}\end{cases}$$

5.1.1 Case 1

In the first case, we run the classical test proposed in [6], dubbed the Gaussian-square-triangle-ellipse test in [9] as its solution contains a Gaussian, a square wave, a triangle and a semi-ellipse wave. The initial condition is

$$u_0(x)=\begin{cases} \frac{1}{6}\big[G(x,\beta,z-\hat{\delta})+4G(x,\beta,z)+G(x,\beta,z+\hat{\delta})\big], & -0.8\le x\le -0.6,\\ 1, & -0.4\le x\le -0.2,\\ 1-\big|10(x-0.1)\big|, & 0.0\le x\le 0.2,\\ \frac{1}{6}\big[F(x,\alpha,a-\hat{\delta})+4F(x,\alpha,a)+F(x,\alpha,a+\hat{\delta})\big], & 0.4\le x\le 0.6,\\ 0, & \text{otherwise,}\end{cases} \tag{5.1}$$

with

$$G(x,\beta,z)=\mathrm{e}^{-\beta(x-z)^2},\qquad F(x,\alpha,a)=\sqrt{\max\big(1-\alpha^2(x-a)^2,0\big)},$$

and $\alpha=10$, $\beta=\frac{\log 2}{36\hat{\delta}^2}$, $z=-0.7$, $a=0.5$, $\hat{\delta}=0.005$.

The solutions at $t=2$ (1 cycle) for $N=200,400,800$ are plotted in Fig. 5 and Fig. 6. As shown in Fig. 5, our results are in agreement with those reported by [9], in which it was indicated that WENO-Z+$^{\mathrm{B}}$ gives a slightly higher resolution than WENO-Z+$^{\mathrm{A}}$ but it is also more oscillatory, although the oscillations can hardly be observed without a very close view. It is worth noting that WENO-IZ+$^{\mathrm{B}}$ can successfully remove these oscillations generated by WENO-Z+$^{\mathrm{B}}$ and preserve very high resolution at the same time. Actually, as shown in Fig. 5 and Fig. 6, WENO-IZ+$^{\mathrm{B}}$ and WENO-IZ+$^{\mathrm{A}}$, as well as WENO-Z+$^{\mathrm{A}}$, have better resolution than WENO-JS, WENO-Z and WENO-Z+I in general, while the difference is not great for short output times. However, if we take a large output time, as shown in Fig. 7(a) in which the results at $t=200$ (100 cycles) for $N=1600$ is presented, we can see that the resolutions of WENO-IZ+$^{\mathrm{A}}$ and WENO-IZ+$^{\mathrm{B}}$ are comparable to that of WENO-Z+$^{\mathrm{A}}$ and they are significantly higher than those of WENO-JS, WENO-Z and WENO-Z+I. Moreover, for a larger output time of $t=2000$ (1000 cycles) with $N=800$, from Fig. 7(b), it can be found that the resolutions of WENO-IZ+$^{\mathrm{A}}$ and WENO-IZ+$^{\mathrm{B}}$ are even much better than that of WENO-Z+$^{\mathrm{A}}$. In addition, the oscillations generated by WENO-Z+$^{\mathrm{B}}$ can be observed very easily for both the two above large output times while WENO-IZ+$^{\mathrm{B}}$ can still avoid these oscillations.

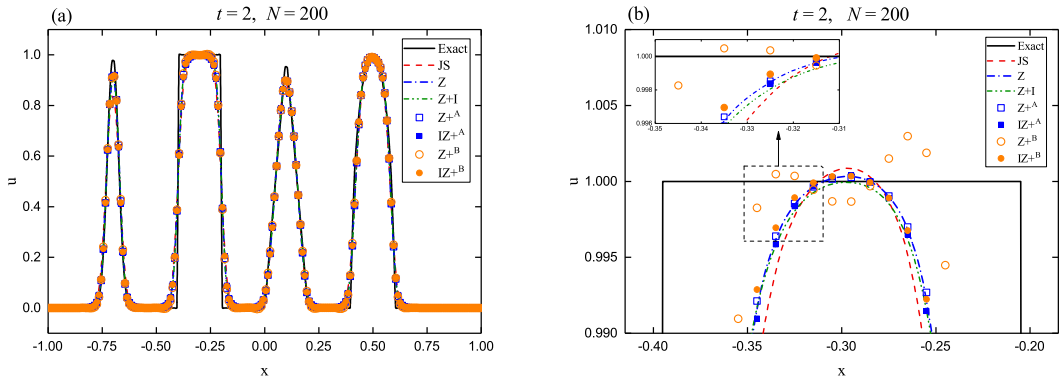

Figure 5: Numerical solutions for the Gaussian-square-triangle-ellipse test at $t=2$ with $N=200$. The right figure gives a zoomed-in view of the square wave.

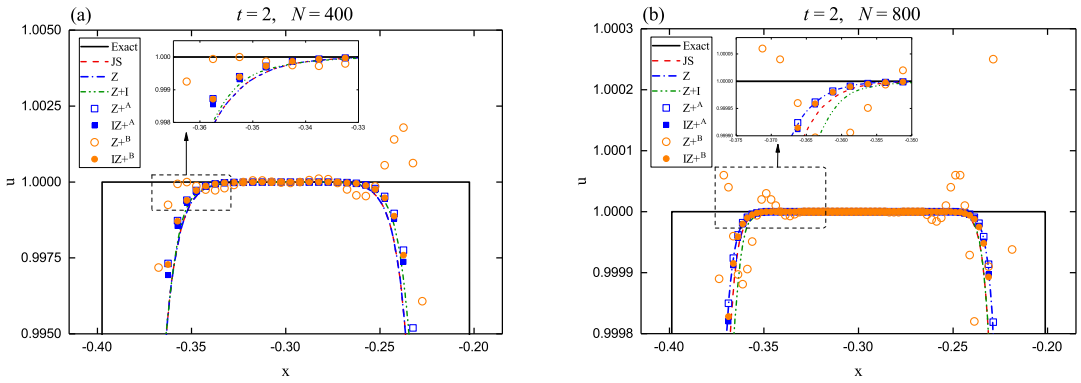

Figure 6: Numerical solutions for the Gaussian-square-triangle-ellipse test at $t=2$ with $N=400,800$. The figures give the zoomed-in views of the square wave.

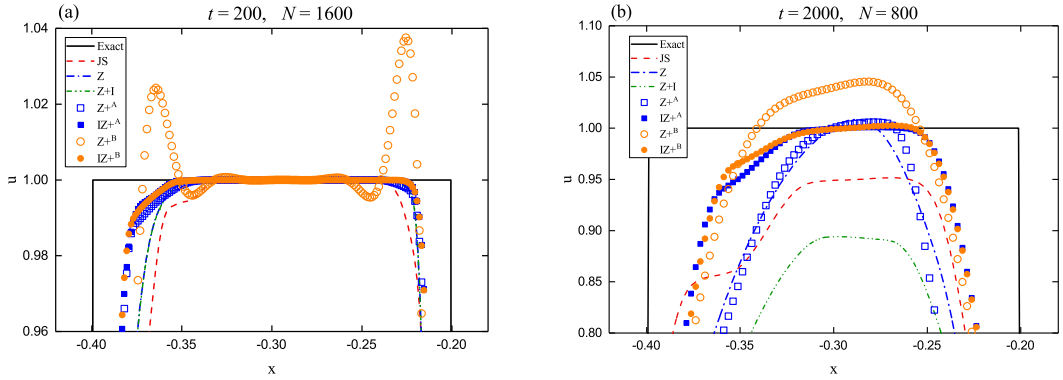

Figure 7: Numerical solutions for the Gaussian-square-triangle-ellipse test at large output times. The figures show the zoomed-in views of the square wave.

Taken together, these results suggest that WENO-IZ+$^{\mathrm{A}}$ and WENO-IZ+$^{\mathrm{B}}$ can successfully avoid spurious oscillations while attaining very high resolutions for problems containing discontinuities for both coarse and refined meshes regardless of the length of output time. This should be a noticeable contribution of the present study.

5.1.2 Case 2

Next, we compute the widely used test [13, 19–21] to demonstrate the competitive advantage of WENO-IZ+$^{\mathrm{A}}$ and WENO-IZ+$^{\mathrm{B}}$ on simulating problems containing high-order critical points for large output times. Its initial condition is as follows

$$u_0(x)=\sin^9(\pi x).$$

Here, the CFL number is set to be $\Delta x^{2/3}$. A large output time of $t=1000$ (500 cycles) and a coarse uniform mesh size of $\Delta x=\frac{1}{100}$ is used.

The numerical solutions are plotted in Figs. 8 and 9. Clearly, WENO-IZ+$^{\mathrm{A}}$ and WENO-IZ+$^{\mathrm{B}}$ greatly outperform WENO-Z+$^{\mathrm{A}}$ and all other considered schemes with the exception of WENO-Z+$^{\mathrm{B}}$ in terms of resolution. As expected, WENO-Z+$^{\mathrm{B}}$ can achieve a remarkably high resolution due to its low dissipation. However, as indicated in [9], WENO-Z+$^{\mathrm{B}}$ is very unstable and it suffers from spurious oscillations in most cases, such as the earlier discussed Gaussian-square-triangle-ellipse test and more one-dimensional Euler tests demonstrated below. Most importantly, we can observe that the resolutions of WENO-IZ+$^{\mathrm{A}}$ and WENO-IZ+$^{\mathrm{B}}$ are comparable to that of WENO-Z+$^{\mathrm{B}}$ on this smooth test case but they can properly prevent the spurious oscillations on the cases with discontinuities.

5.2 1D Euler equations

The 1D Euler equations in strong conservation form are defined by

$$\begin{pmatrix}\rho\\ \rho u\\ E\end{pmatrix}_t+\begin{pmatrix}\rho u\\ \rho u^2+p\\ uE+up\end{pmatrix}_x=\mathbf{0},$$

where ρ, u, p, E are the density, velocity, pressure and total energy, respectively. The following equation of state for an ideal polytropic gas

$$p=(\gamma-1)\left(E-\frac{1}{2}\rho u^2\right),\quad \gamma=1.4,$$

is supplemented to close the governing equations of one-dimensional Euler system.

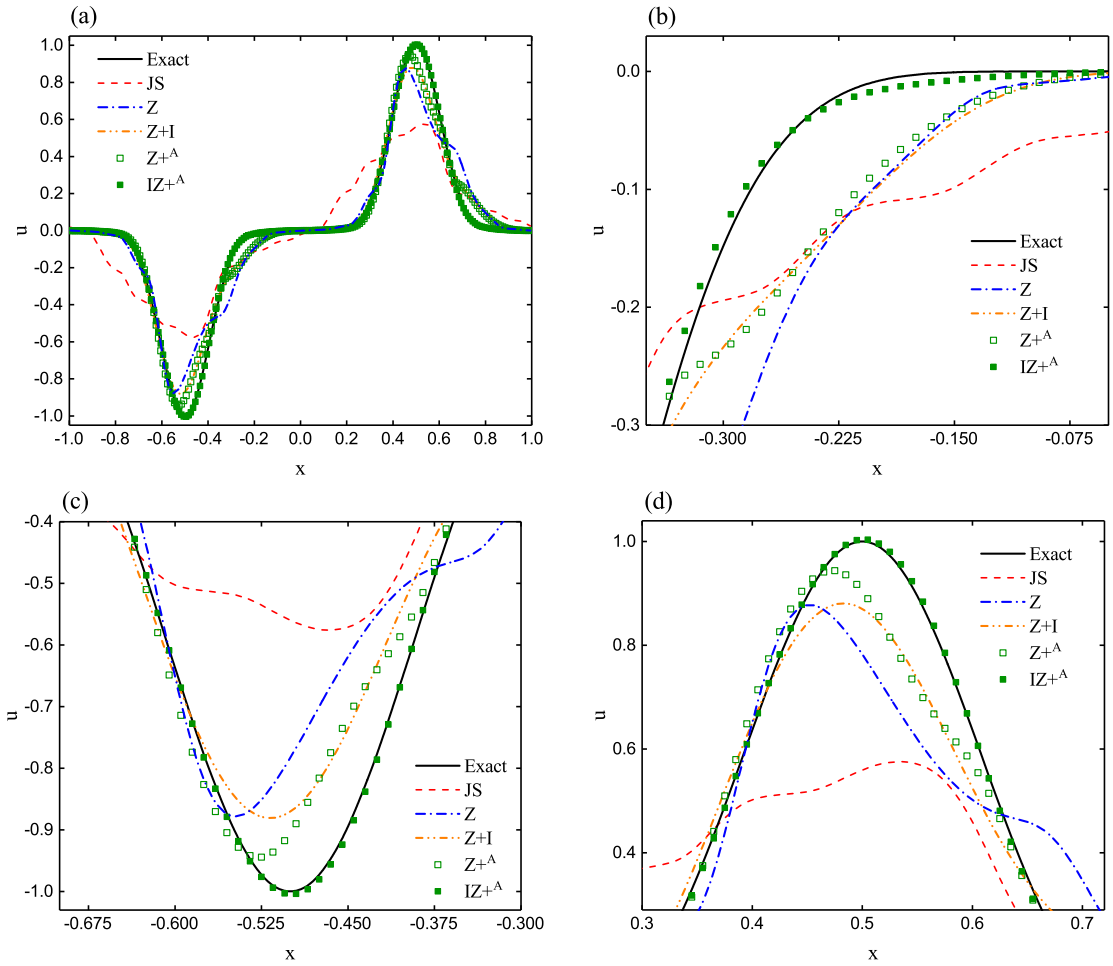

Figure 8: Performance of WENO-IZ+^{A}, WENO-Z+^{A}, WENO-JS, WENO-Z and WENO-Z+I for $u_0(x)=\sin^9(x)$ at $t=1000$ with $N=200$.

5.2.1 Riemann initial value problem of Sod

The initial condition for this standard shock tube problem [38] is given by

$$(\rho,u,p)(x,0)=\begin{cases}(1.0,0.0,1.0), & x\in[0.0,0.5],\\ (0.125,0.0,0.1), & x\in[0.5,1.0].\end{cases}$$

The zero-gradient boundary conditions are used and the calculations are conducted with $t=0.25$ and $N=300$.

The simulated density profiles are shown in Fig. 10. Generally speaking, all the considered schemes perform well at contact discontinuity and shock. However, closer inspection reveals that WENO-Z+^{A} and WENO-Z+^{B}, as well as WENO-Z+I, generate ev-

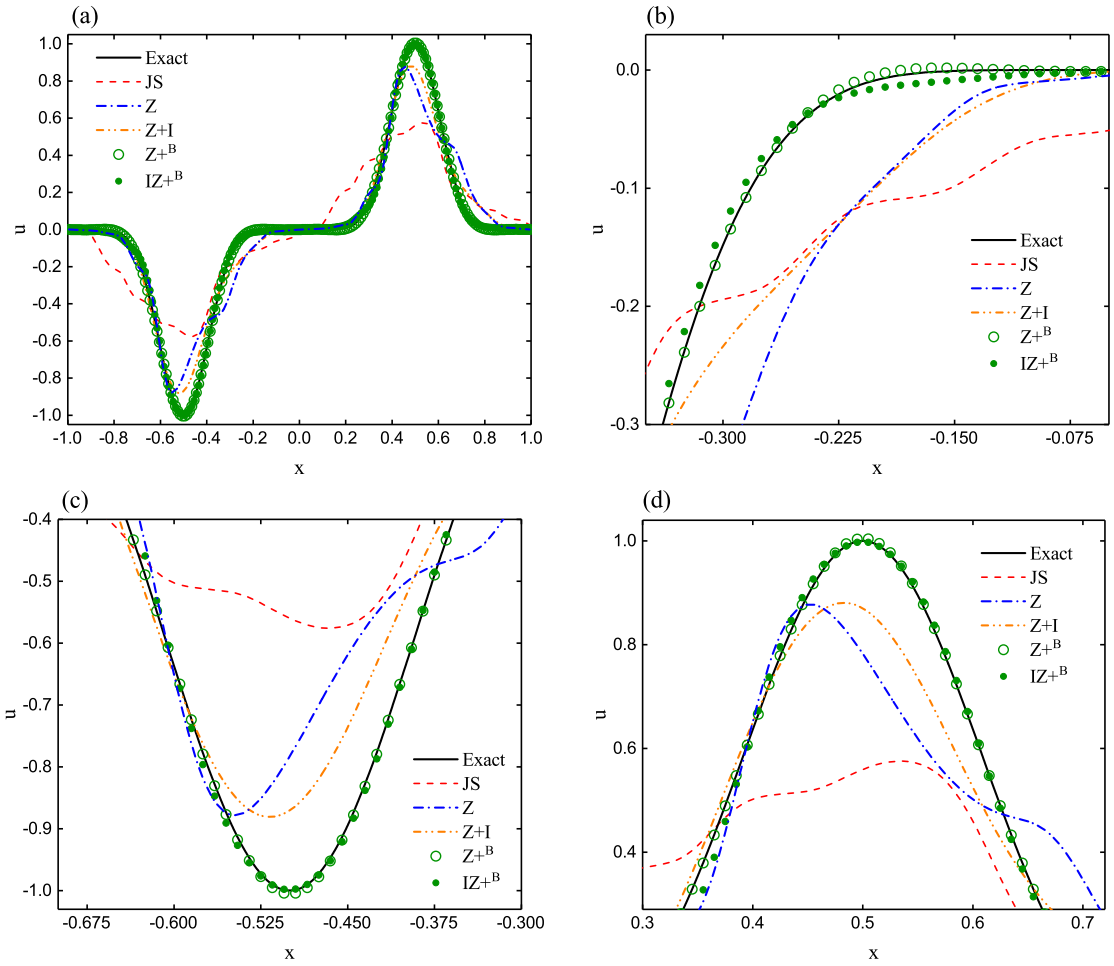

Figure 9: Performance of WENO-IZ+^{B}, WENO-Z+^{B}, WENO-JS, WENO-Z and WENO-Z+I for $u_0(x)=\sin^9(x)$ at $t=1000$ with $N=200$.

ident spurious oscillations. The result of WENO-Z also seems to be oscillatory, albeit in a smaller scale. It can be seen that WENO-IZ+^{A} and WENO-IZ+^{B}, as well as WENO-JS, can successfully prevent these spurious oscillations, while the solutions of WENO-IZ+^{A} and WENO-IZ+^{B} get closer to the exact solution than that of WENO-JS.

5.2.2 Riemann initial value problem of Lax

For the Lax problem [31], the initial condition is set as

$$(\rho,u,p)(x,0)=\begin{cases}(0.445,0.698,3.528), & x\in[-5,0],\\ (0.500,0.000,0.571), & x\in[0,5].\end{cases}$$

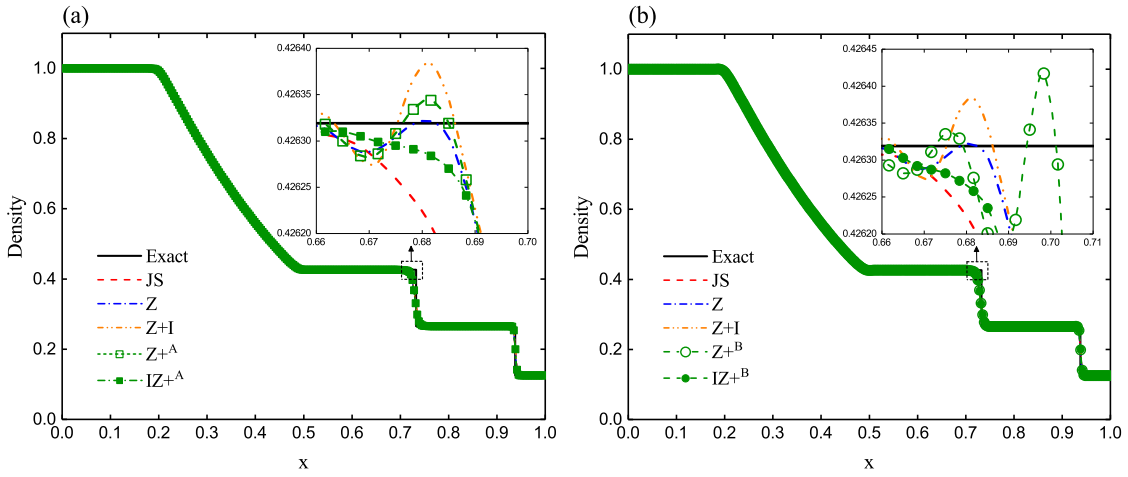

Figure 10: Numerical solutions of the Sod's Riemann initial value problem with $t=0.25$ and $N=300$.

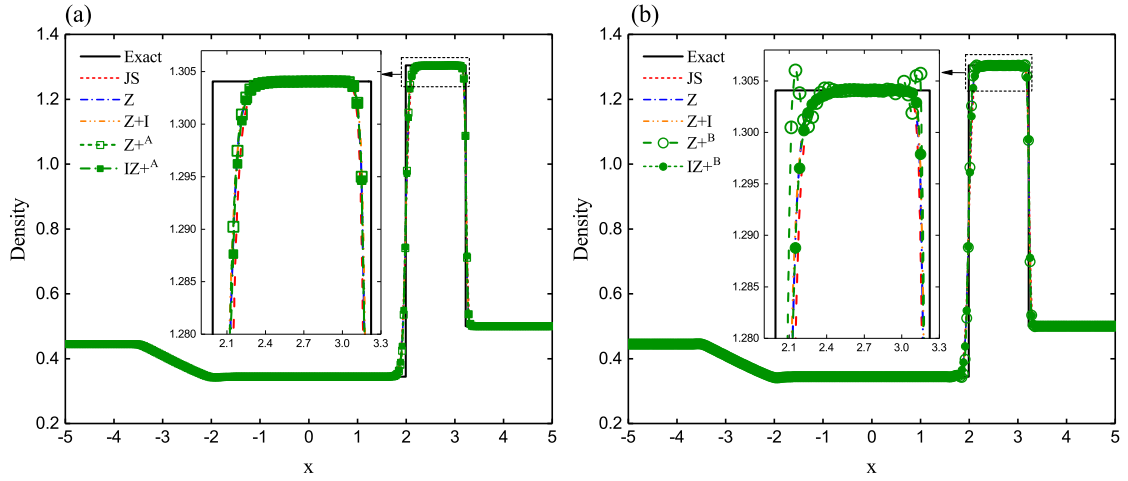

Figure 11: Numerical solutions of the Lax's Riemann initial value problem with $t=1.3$ and $N=300$.

The zero-gradient boundary conditions are used and the calculations are conducted with $t=1.3$ and $N=300$.

The simulated density profiles are shown in Fig. 11. As before, close examination shows that WENO-Z+$^{\mathrm{B}}$ produces unfavorable spurious oscillations while WENO-IZ+$^{\mathrm{B}}$ can successfully remove them. For this test, the other considered schemes can also avoid spurious oscillations and their performances are nearly the same as that of WENO-IZ+$^{\mathrm{B}}$.

5.2.3 Shock-density wave interaction of Shu-Osher

For this Mach 3 shock-density wave interaction [27], the initial condition is specified by

$$(\rho,u,p)(x,0)=\begin{cases}(3.857143,2.629369,10.333333), & -5.0\leq x\leq -4.0,\\ (1.0+0.2\sin(5x),0,1), & -4.0\leq x\leq 5.0.\end{cases}$$

The zero-gradient boundary conditions are used and the calculations are conducted with $t=1.8$ and $N=300$.

The simulated density profiles are plotted in Fig. 12 and Fig. 13. The result computed by WENO-JS with a refined mesh of N=10000 was used as the reference solution. Clearly, WENO-JS shows the lowest resolution. We can see that the solutions of WENO-IZ+^{A}, WENO-IZ+^{B}, WENO-Z+^{A}, WENO-Z+^{B} and WENO-Z+I are almost the same, and have better resolution near shocklets and high-frequency waves behind the main shock than that of WENO-Z.

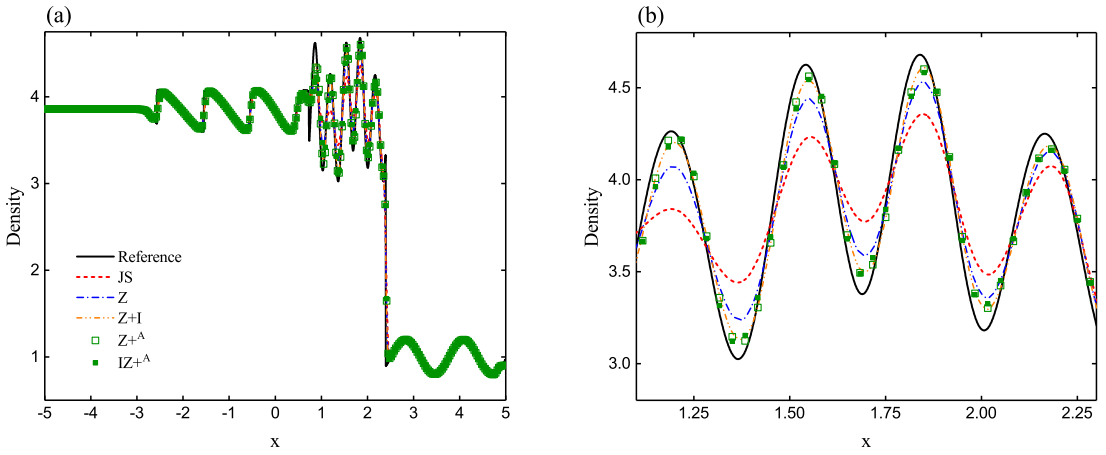

Figure 12: Numerical solutions of the Shu-Osher's shock-density wave interaction with $t=1.8$ and $N=300$, for WENO-IZ+^{A}.

5.2.4 Shock-density wave interaction of Titarev-Toro

This is a more severe version [28–30] of the previous example. Its computational domain is initialized by

$$(\rho,u,p)(x,0)=\begin{cases}(1.515695,0.523346,1.805000), & x\in[-5.0,-4.5],\\ (1.0+0.1\sin(20\pi x),0,1), & x\in[-4.5,5.0].\end{cases}$$

The zero-gradient boundary conditions are used and the calculations are conducted with $t=5.0$ and $N=1500$.

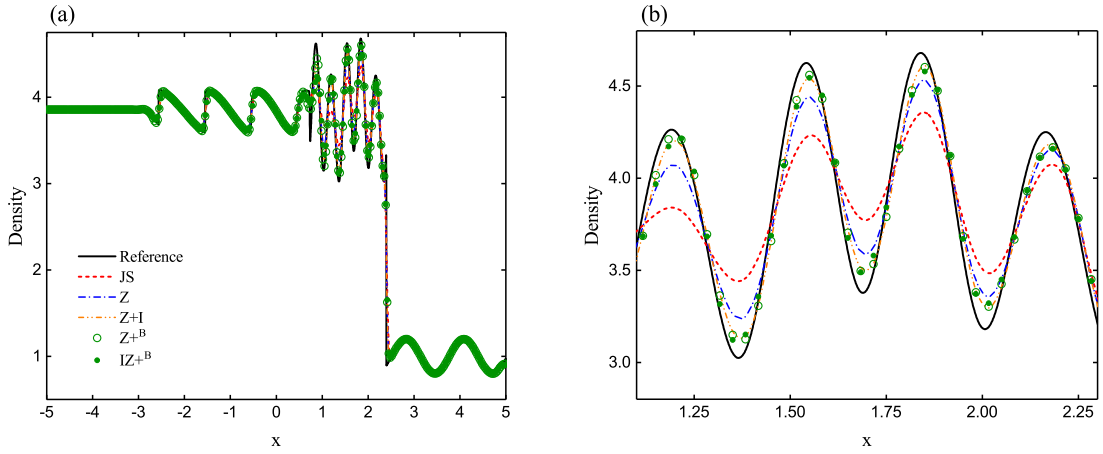

Figure 13: Numerical solutions of the Shu-Osher's shock-density wave interaction with $t=1.8$ and $N=300$, for WENO-IZ+^{B}.

The simulated density profiles are plotted in Fig. 14 and Fig. 15. Also, the result computed by WENO-JS with a refined mesh of $N=10000$ was used as the reference solution. As before, the resolution of WENO-JS is the lowest, followed by that of WENO-Z. WENO-IZ+^{A} shows good agreement with WENO-Z+I and its resolution is significantly higher than those of WENO-Z+^{A} and WENO-Z+^{B}. Moreover, WENO-IZ+^{B} shows the best description near shocklets and high-frequency waves, even slightly better than those of WENO-IZ+^{A} and WENO-Z+I. It is worthy of note that, as shown in Fig. 15(c), WENO-Z+^{B} falsely amplifies the smooth waves behind the high-frequency waves while WENO-IZ+^{B} can properly fix this issue.

5.2.5 Interacting blast wave problem

The initial condition is given by [39]

$$(\rho,u,p)(x,0)=\begin{cases}(1,0,1000), & x\in[0,0.1),\\ (1,0,0.01), & x\in[0.1,0.9),\\ (1,0,100), & x\in[0.9,1.0].\end{cases}$$

The reflective boundary conditions are used and the calculations are conducted with $t=0.038$ and $N=300$.

The simulated density profiles are plotted in Fig. 16 and Fig. 17. The reference solution is obtained by WENO-JS with $N=10000$. Although this problem is much more stringent than those discussed previously, the new proposed WENO-IZ+^{A} and WENO-IZ+^{B}, as well as other considered WENO schemes, still work well here. It can be observed that WENO-IZ+^{A} and WENO-IZ+^{B} perform as excellently as WENO-Z+^{A}, WENO-Z+^{B} and WENO-Z, all of which are less dissipative than WENO-JS. WENO-Z+I appears to be slightly better than all other schemes for this test.

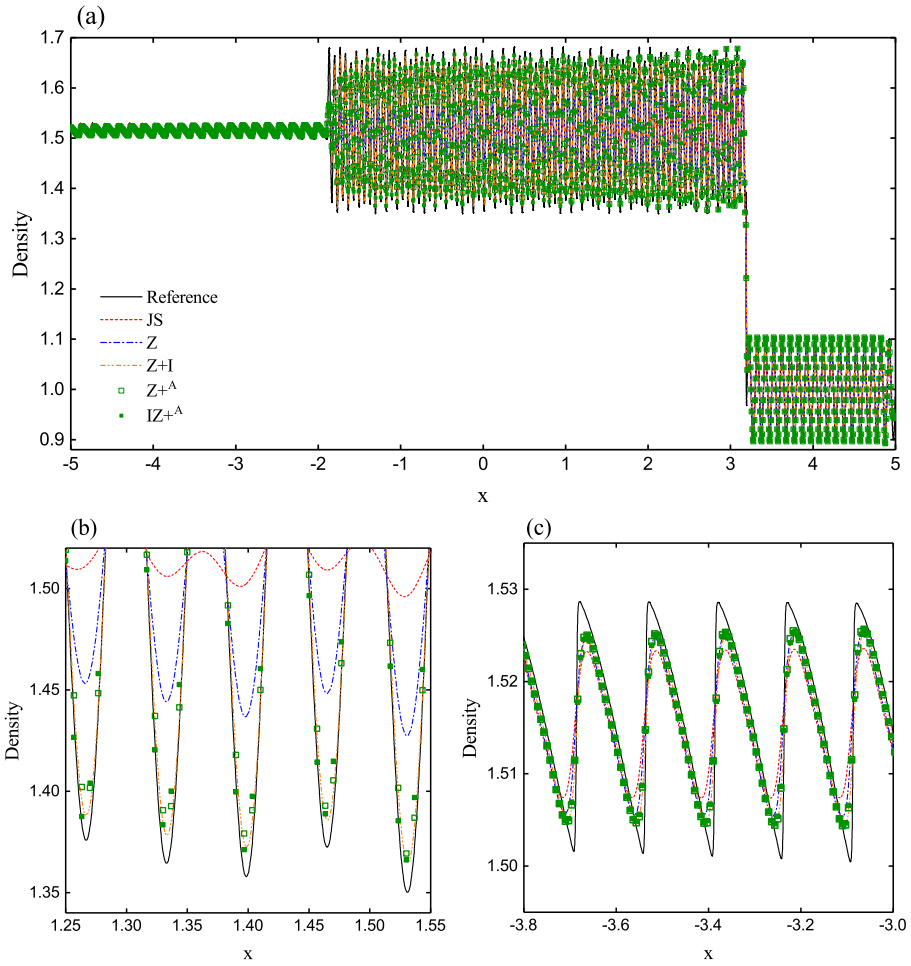

Figure 14: Numerical solutions of the Titarev-Toro's shock-density wave interaction with $t=5.0$ and $N=1500$, for WENO-IZ+^{A}.

5.3 2D Euler equations

The 2D Euler equations in strong conservation form are defined by

$$\begin{pmatrix} \rho \\ \rho u \\ \rho v \\ E \end{pmatrix}_t + \begin{pmatrix} \rho u \\ \rho u^2+p \\ \rho uv \\ uE+up \end{pmatrix}_x + \begin{pmatrix} \rho v \\ \rho vu \\ \rho v^2+p \\ vE+vp \end{pmatrix}_y = \mathbf{0}.$$

Here, v stands for the velocity in the y coordinate direction. Similarly,

$$p=(\gamma-1)\left[E-\frac{1}{2}\rho\left(u^2+v^2\right)\right]$$

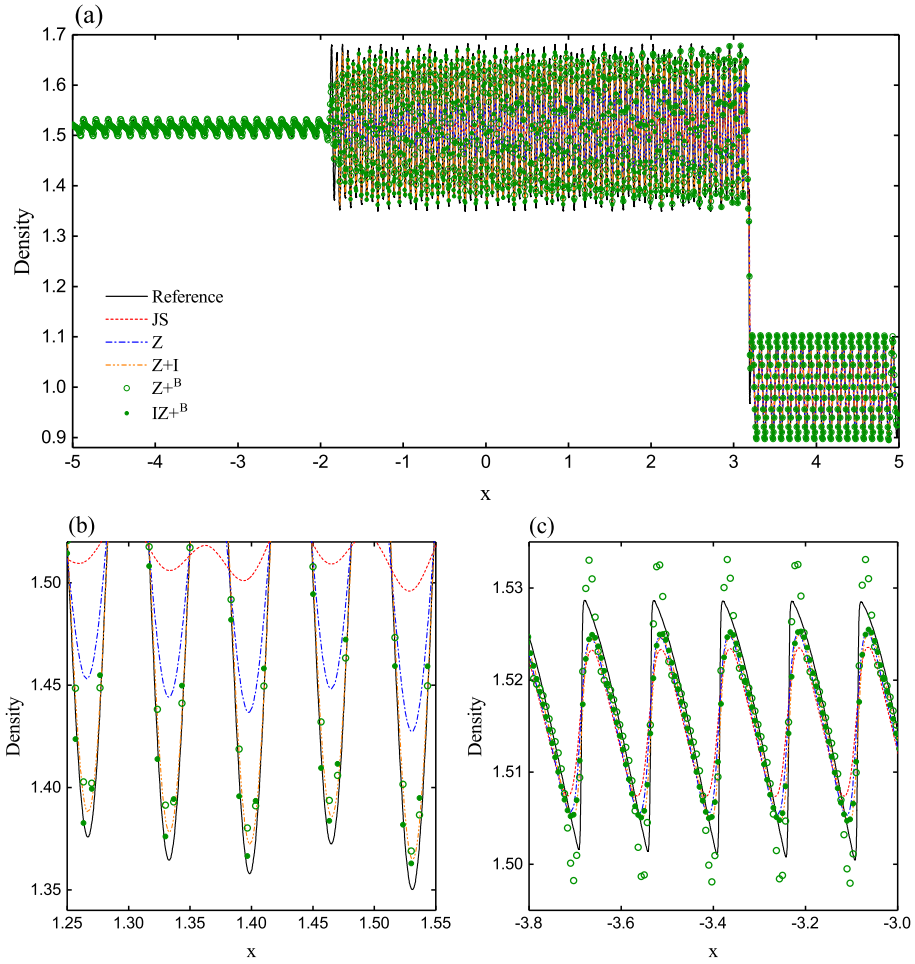

Figure 15: Numerical solutions of the Titarev-Toro's shock-density wave interaction with $t=5.0$ and $N=1500$, for WENO-IZ+^{B}.

is supplemented to close the governing equations of two-dimensional Euler system. Unless otherwise indicated, $\gamma=1.4$ is used in all tests of this subsection.

5.3.1 2D shock-density wave interaction

Now, we simulate the 2D versions of the Shu-Osher's and Titarev-Toro's shock-density wave interaction discussed earlier. Their initial conditions are given as

$$(\rho,u,v,p)(x,y,0)=\begin{cases}(3.857143,2.629369,0,10.333333), & x\in(-5,-4),\\ \left(1.0+0.2\sin\left(5x\cos\dfrac{\pi}{6}+5y\sin\dfrac{\pi}{6}\right),0,0,1\right), & x\in[-4,5),\end{cases}$$

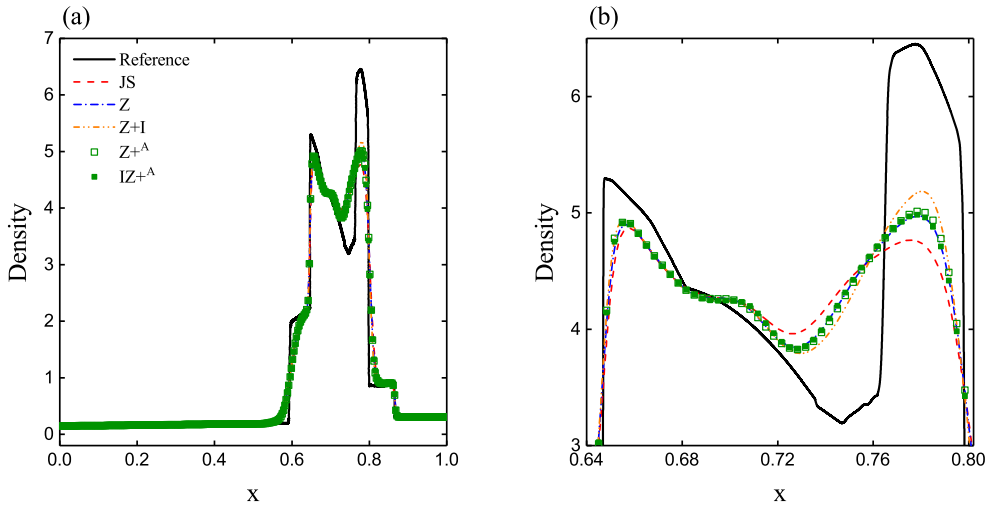

Figure 16: Numerical solutions of the interacting blast wave problem with $t=0.038$ and $N=300$, for WENO-IZ+^{A}.

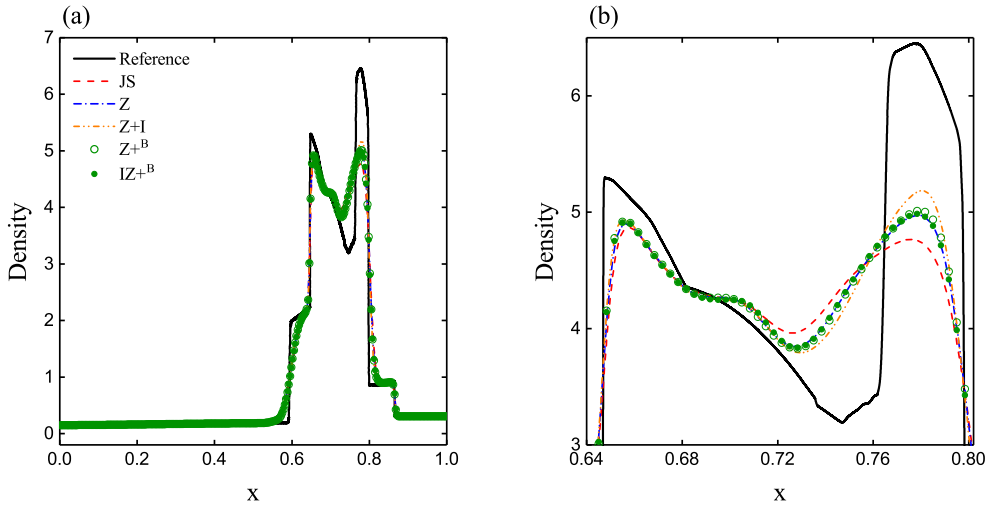

Figure 17: Numerical solutions of the interacting blast wave problem with $t=0.038$ and $N=300$, for WENO-IZ+^{B}.

and

$$(\rho,u,v,p)(x,y,0)=\begin{cases}(1.515695,0.523346,0,1.805000), & x\in(-5,-4.5),\\ \left(1.0+0.1\sin\left(20\pi x\cos\frac{\pi}{6}+20\pi y\sin\frac{\pi}{6}\right),0,0,1\right), & x\in[-4.5,5).\end{cases}$$

The transmissive boundary conditions are used at the left and right boundaries and the periodic conditions are used at the top and bottom boundaries.

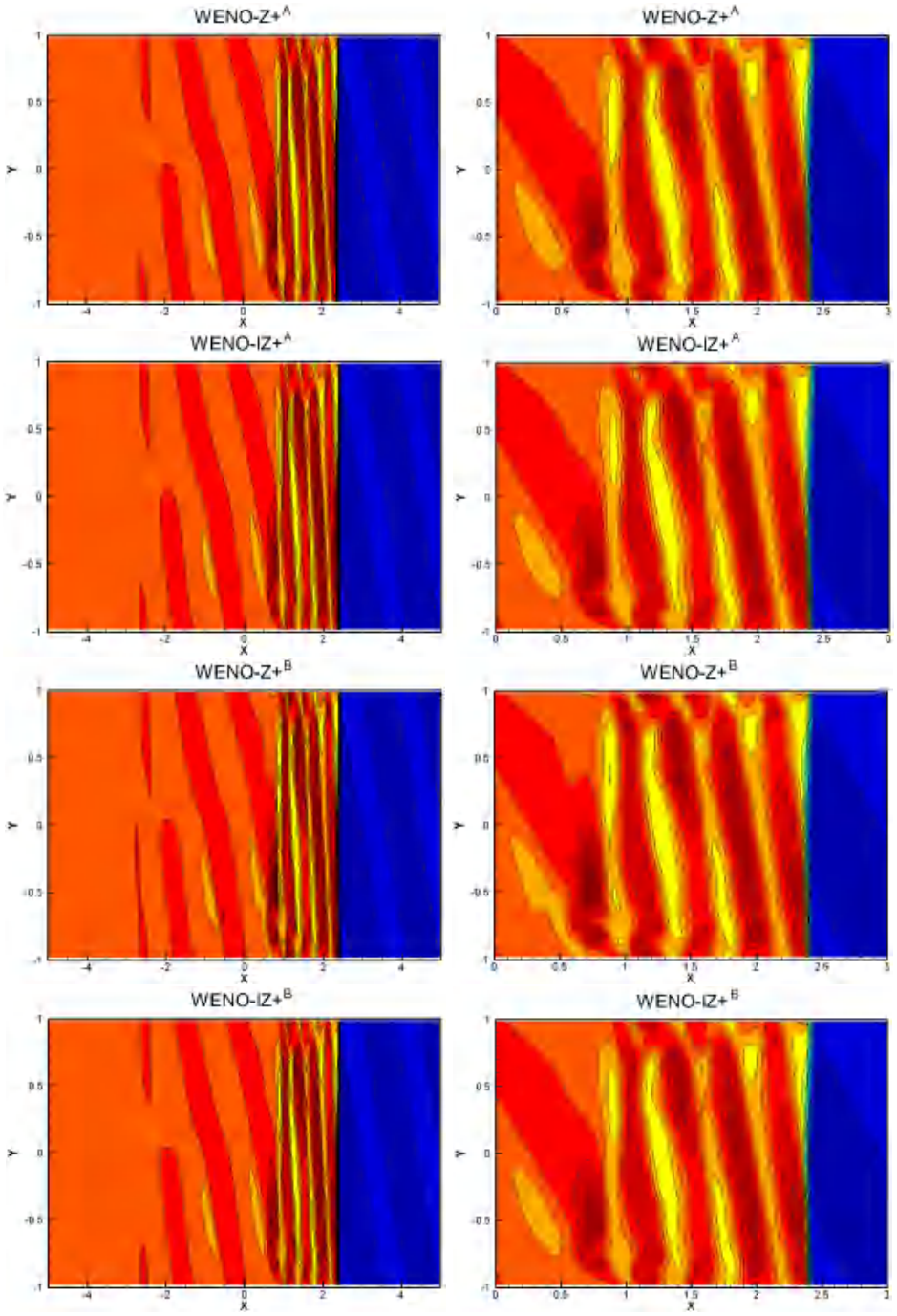

Figure 18: Numerical solutions of the 2D Shu-Osher's shock-density wave interaction with $t=1.8$ and $N_x\times N_y=300\times 60$.

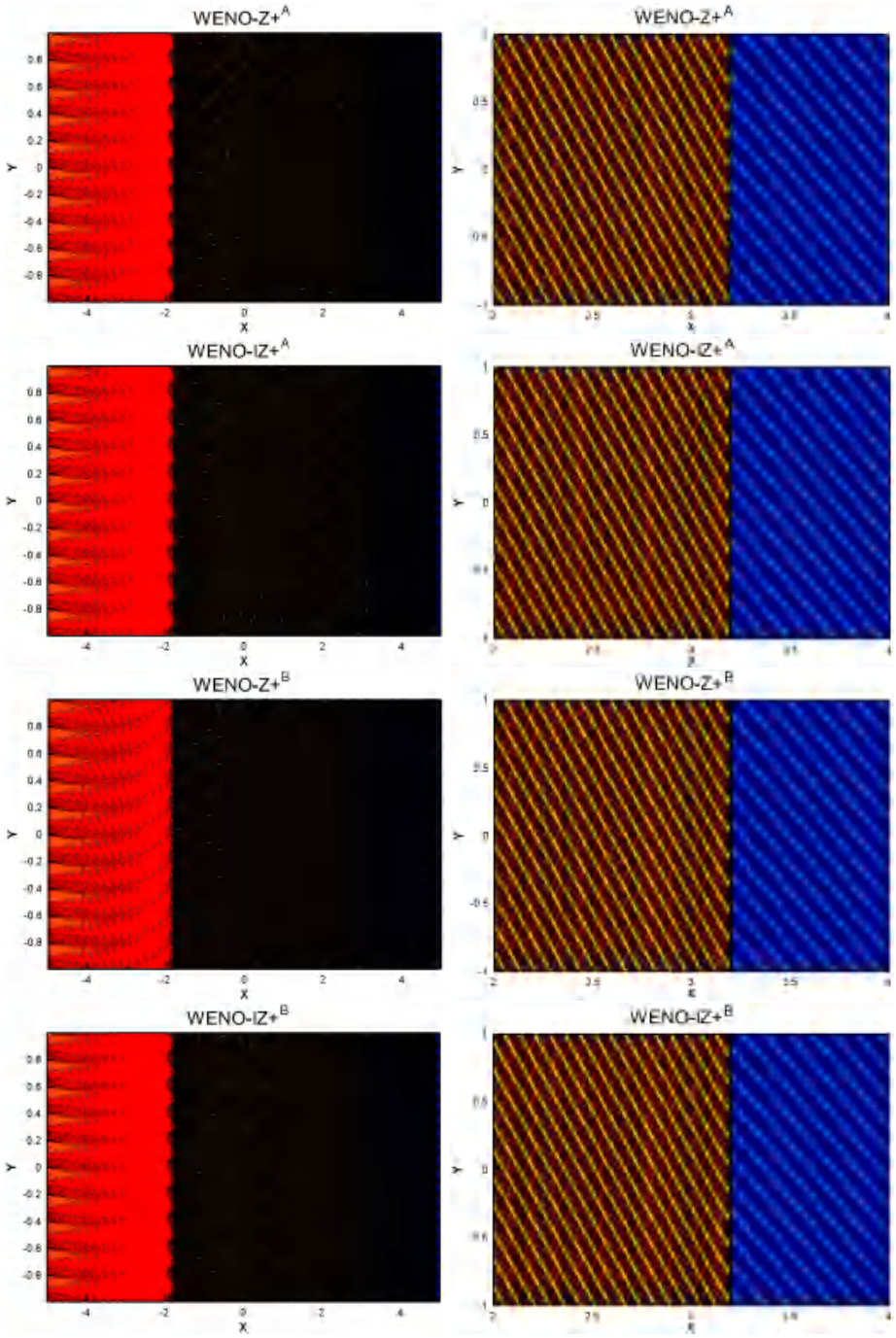

Figure 19: Numerical solutions of the 2D shock-density wave interaction of Titarev-Toro with 20 equally spaced contour lines from 0.9 to 1.65 using $N_x \times N_y = 1500 \times 300$ cells at $t = 5.0$.

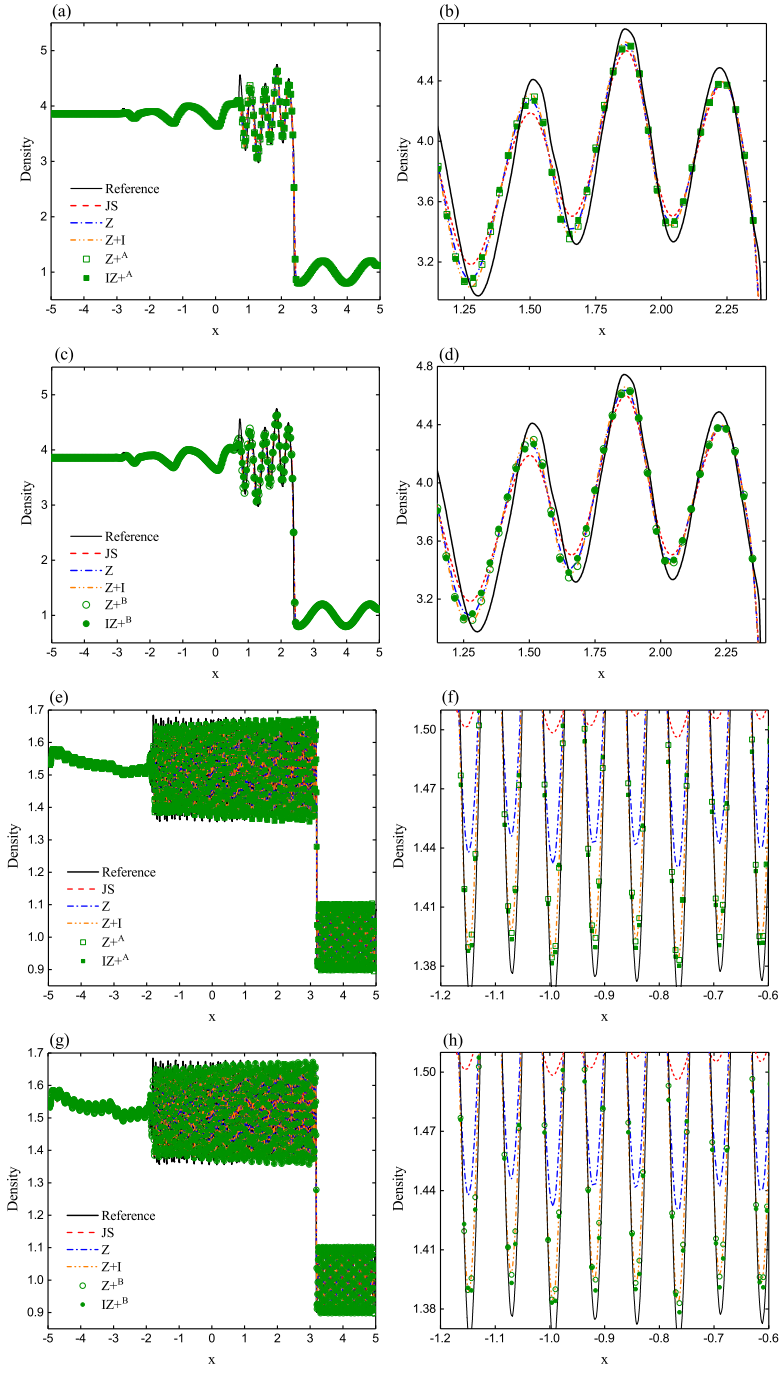

Figure 20: The cross-sectional slices of density plot along the plane $y = 0.0$ for the 2D shock-density wave interaction of Shu-Osher (the first two rows) and Titarev-Toro (the last two rows). The right figures show a zoom of the left ones.

Fig. 18 shows the density contours of the 2D Shu-Osher's shock-density wave interaction with $t=1.8$ and $N_x\times N_y=300\times 60$. Fig. 20 gives the cross-sectional slices of density plot along the plane $y=0.0$ of WENO-Z+$^{\rm A}$, WENO-Z+$^{\rm B}$, WENO-IZ+$^{\rm A}$ and WENO-IZ+$^{\rm B}$. For the purpose of comparison, the results of WENO-JS, WENO-Z, WENO-Z+I and refined WENO-IZ+$^{\rm B}$ (reference solution) are also plotted. We can see that WENO-IZ+$^{\rm A}$ and WENO-IZ+$^{\rm B}$ provide almost comparable results to those of WENO-Z+$^{\rm A}$, WENO-Z+$^{\rm B}$, WENO-Z and WENO-Z+I, which perform better than WENO-JS.

Fig. 19 shows the density contours of the 2D Titarev-Toro's shock-density wave interaction with $t=5.0$ and $N_x\times N_y=1500\times 300$. And also, we plot the density profiles on the $y=0.0$ cross-sectional plane as shown in Fig. 20. Like the 1D case, the resolution of WENO-JS is lowest, followed by WENO-Z. Close examination indicates that WENO-IZ+$^{\rm A}$ and WENO-IZ+$^{\rm B}$ again perform slightly better than WENO-Z+$^{\rm A}$, WENO-Z+$^{\rm B}$ and even WENO-Z+I.

5.3.2 Shock-vortex interaction

The computational domain of the commonly used shock-vortex interaction problem [40–42] is $[0,1]\times[0,1]$ and it is initialized by

$$(\rho,u,v,p)(x,y,0)=\begin{cases}(\rho_{\rm L}+\delta\rho,u_{\rm L}+\delta u,v_{\rm L}+\delta v,p_{\rm L}+\delta p), & x<0.5,\\ (\rho_{\rm R},u_{\rm R},v_{\rm R},p_{\rm R}), & x\geq 0.5,\end{cases}$$

where $\rho_{\rm L}=1$, $u_{\rm L}=\sqrt{\gamma}$, $v_{\rm L}=0$, $p_{\rm L}=1$, $v_{\rm R}=0$, $p_{\rm R}=1.3$ and

$$\rho_{\rm R}=\rho_{\rm L}\left(\frac{\gamma-1+(\gamma+1)p_{\rm R}}{\gamma+1+(\gamma-1)p_{\rm R}}\right),\qquad u_{\rm R}=u_{\rm L}\left(\frac{1-p_{\rm R}}{\sqrt{\gamma-1+p_{\rm R}(\gamma+1)}}\right),$$

$$\delta\rho=\frac{\rho_{\rm L}^2}{(\gamma-1)p_{\rm L}}\delta T,\quad \delta u=\hat{\epsilon}\frac{y-y_{\rm c}}{r_{\rm c}}{\rm e}^{\alpha(1-r^2)},\quad \delta v=-\hat{\epsilon}\frac{x-x_{\rm c}}{r_{\rm c}}{\rm e}^{\alpha(1-r^2)},\quad \delta p=\frac{\gamma\rho_{\rm L}^2}{(\gamma-1)\rho_{\rm L}}\delta T,$$

with

$$\begin{aligned}&\hat{\epsilon}=0.3,\alpha=0.204,\\ &x_{\rm c}=0.25,y_{\rm c}=0.5,r_{\rm c}=0.05,\\ &r=\sqrt{((x-x_{\rm c})^2+(y-y_{\rm c})^2)/r_{\rm c}^2},\\ &\delta T=-(\gamma-1)\hat{\epsilon}^2{\rm e}^{2\alpha(1-r^2)}/(4\alpha\gamma).\end{aligned}$$

The transmissive boundary conditions are used for all boundaries and the calculations are conducted with $N_x\times N_y=800\times 800$.

Fig. 21 presents the density contours of the shock-vortex interaction problem computed by WENO-Z, WENO-Z+I, WENO-Z+$^{\rm A}$, WENO-IZ+$^{\rm A}$, WENO-Z+$^{\rm B}$ and WENO-IZ+$^{\rm B}$ at $t=0.35$. Firstly, it can be seen that all considered schemes can properly capture the main structure of the complicated flow after the interaction. However, after careful observation, we can find that WENO-Z+I suffers from severe post-shock oscillations

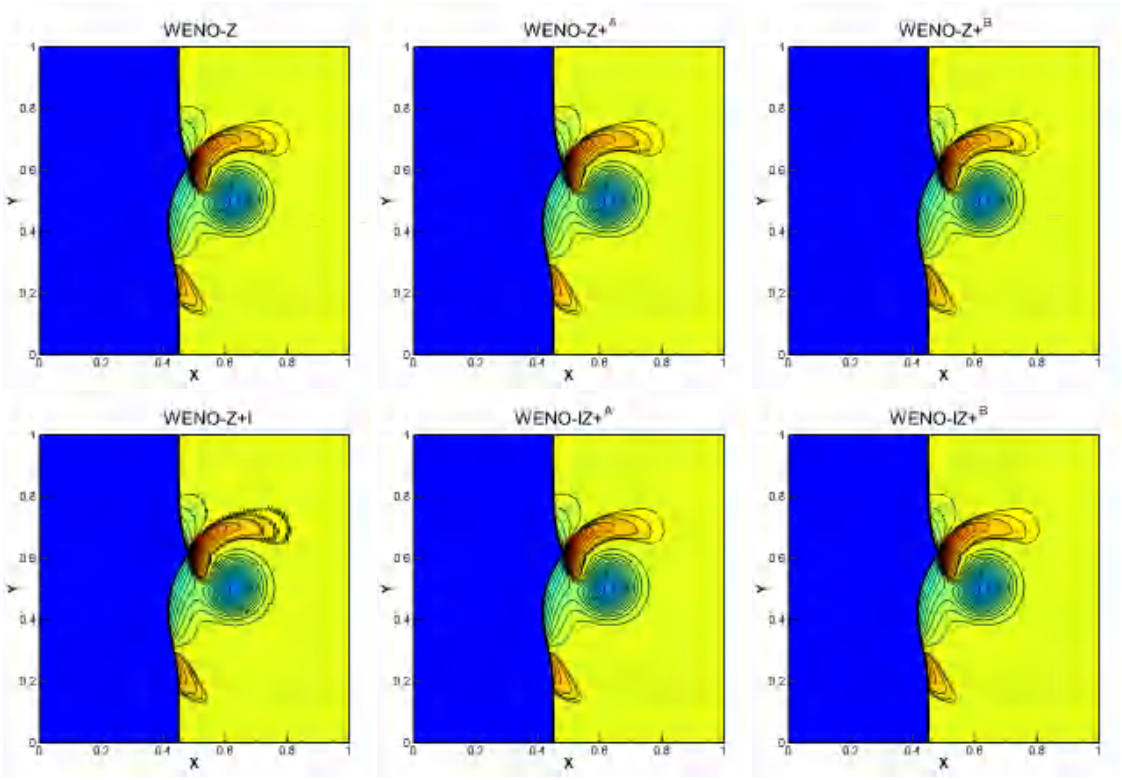

Figure 21: Numerical solutions of the shock-vortex interaction with 50 equally spaced contour lines from 0.9 to 1.4 using $N_x \times N_y = 800 \times 800$ cells at $t = 0.35$.

which can also be observed, although not as severe as that of WENO-Z+I, in the solutions of WENO-Z, WENO-Z+$^{\mathrm{A}}$ and WENO-Z+$^{\mathrm{B}}$. It is noticeable that WENO-IZ+$^{\mathrm{A}}$ and WENO-IZ+$^{\mathrm{B}}$ can remove or greatly reduce these post-shock oscillations, and this can be observed more clearly in the cross-sectional slices of density plot along the plane $y = 0.65$ as shown in Fig. 22, in which the reference solution is obtained by using WENO-JS with $N_x \times N_y = 1600 \times 1600$ uniform meshes.

5.3.3 2D Riemann problem

The 2D Riemann problem has been widely used to test the performance of high-resolution numerical schemes [44,45] since it was firstly introduced by [43]. Here, we consider Configuration 9 of [44]. Its computational domain of $[0,1] \times [0,1]$ is divided into four quadrants by lines $x = 0.5$ and $y = 0.5$ and these quadrants are specified by the following initial

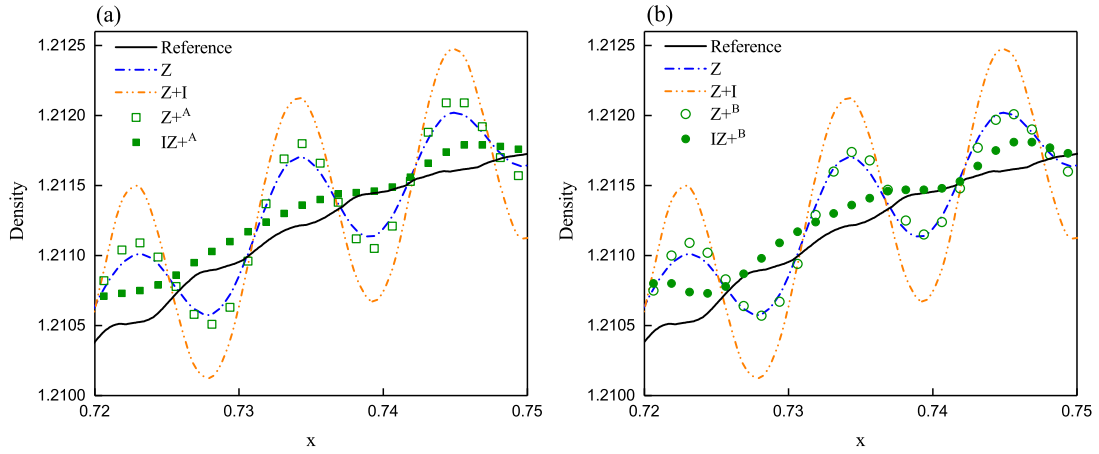

Figure 22: The cross-sectional slices of density plot along the plane $y=0.65$ for the shock-vortex interaction problem using $N_x\times N_y=800\times 800$ cells at $t=0.35$. The figures show a zoom over $x\in[0.72,0.75]$.

constant states

$$(\rho,u,v,p)(x,y,0)=\begin{cases}(1.0,0.0,0.3,1.0), & 0.5\le x\le 1.0, \quad 0.5\le y\le 1.0,\\ (2.0,0.0,-0.3,1.0), & 0.0\le x\le 0.5, \quad 0.5\le y\le 1.0,\\ (1.039,0.0,-0.8133,0.4), & 0.0\le x\le 0.5, \quad 0.0\le y\le 0.5,\\ (0.5197,0.0,-0.4259,0.4), & 0.5\le x\le 1.0, \quad 0.0\le y\le 0.5.\end{cases}$$

On all boundaries, the transmission boundary conditions are used.

Fig. 23 plots the density contours with a spatial resolution $N_x\times N_y=800\times 800$ at $t=0.3$. As expected, WENO-IZ+$^{\rm A}$ can considerably reduce the post-shock numerical oscillations while the other schemes generate evident oscillations. Again, WENO-IZ+$^{\rm B}$ also generates oscillations. However, it is less oscillatory than WENO-Z+$^{\rm B}$ and its oscillation is only severer than that of WENO-IZ+$^{\rm A}$ but better than those of all other considered schemes.

5.3.4 Rayleigh-Taylor instability

This is a famous 2D benchmark test [12,20,46,47]. The initial condition is given by

$$(\rho,u,v,p)(x,y,0)=\begin{cases}(2,0,-0.025c\cdot\cos(8\pi x),2y+1), & y\le 0.5,\\ (1,0,-0.025c\cdot\cos(8\pi x),y+1.5), & y>0.5.\end{cases}$$

Here, the ratio of specific heats is specified as $\gamma=5/3$ and $c=\sqrt{\gamma p/\rho}$ is the speed of sound. The reflective boundary conditions are used on boundaries $x=0,0.25$. On boundaries $y=0,1$, the following values are assigned

$$(\rho,u,v,p)(x,y,t)=\begin{cases}(2,0,0,1), & y=0,\\ (1,0,0,2.5), & y=1.\end{cases}$$

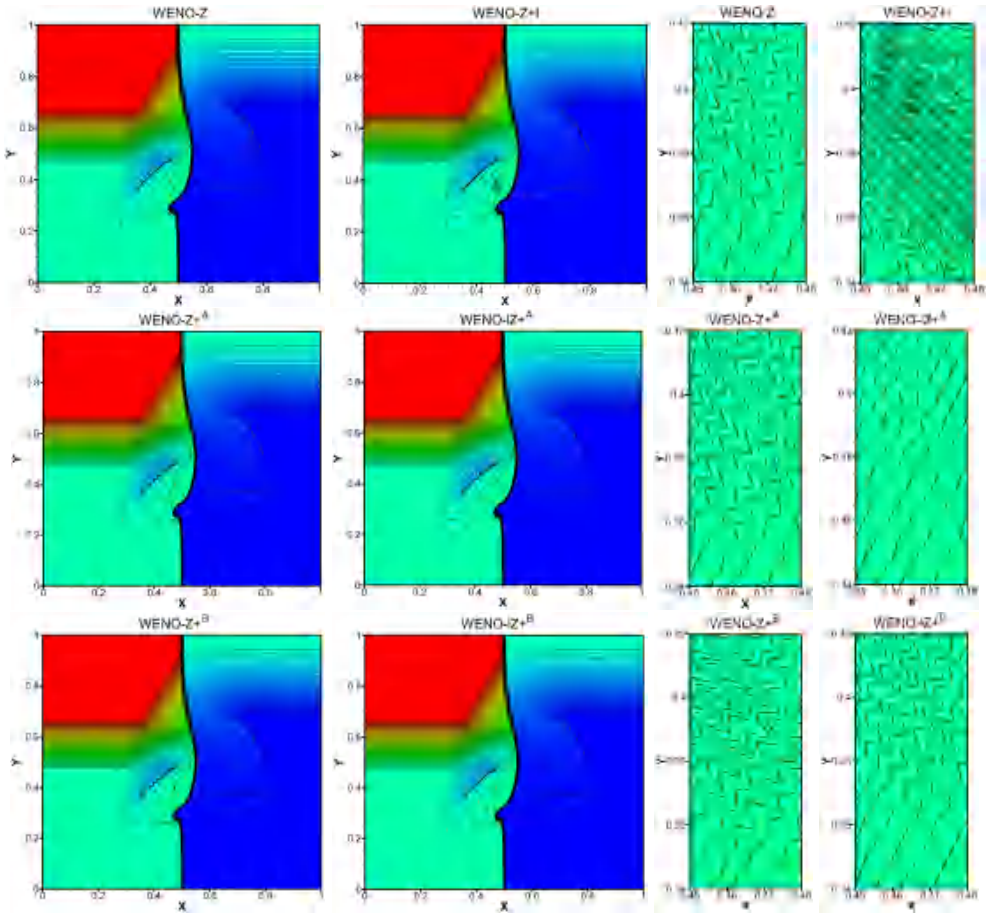

Figure 23: Numerical solutions of the 2D Riemann problem using $N_x \times N_y = 800 \times 800$ cells at $t = 0.3$. The last two columns show a zoom over the regions with severe post-shock oscillations.

The density contours with a spatial resolution $N_x \times N_y = 240 \times 960$ at $t = 1.98$ are shown in Fig. 24. Clearly, the WENO-IZ+$^{\mathrm{A}}$ and WENO-IZ+$^{\mathrm{B}}$ obtain more complex structures than WENO-JS and WENO-Z. WENO-Z+$^{\mathrm{A}}$, WENO-Z+$^{\mathrm{B}}$ and WENO-Z+I also produce finer structures.

5.3.5 Double Mach reflection

The computational domain of the double Mach reflection problem [39] is specified by

$$(\rho,u,v,p)(x,y,0) = \begin{cases} (8.0, 8.25\cos\theta, -8.25\sin\theta, 116.5), & x < x_0 + \dfrac{y}{\sqrt{3}}, \\ (1.4, 0.0, 0.0, 1.0), & x \geq x_0 + \dfrac{y}{\sqrt{3}}, \end{cases}$$

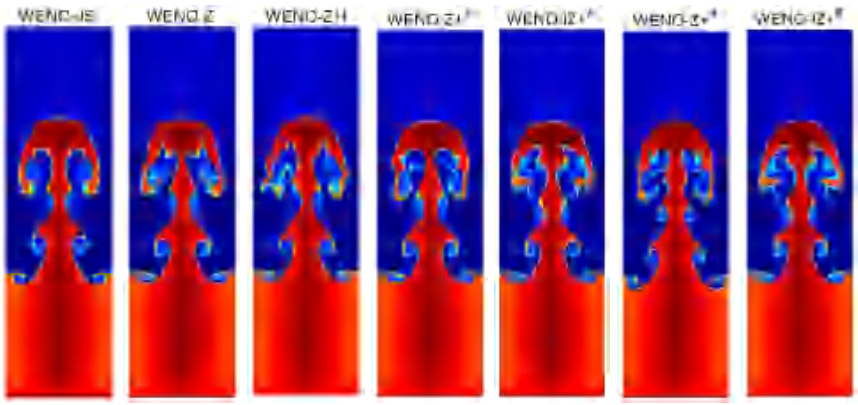

Figure 24: Numerical solutions of the Rayleigh-Taylor instability with $t=1.98$ and $N_x\times N_y=240\times 960$.

with $x_0=\frac{1}{6}$ and $\theta=\frac{\pi}{6}$. At the right edge, the zero-gradient outflow condition is utilized. At the left edge, the boundary is assigned with the post-shock values as given above, and the region over $[0,\frac{1}{6})$ along the bottom boundary is also always assigned with these post-shock values. The region over $[\frac{1}{6},4]$ is a reflecting wall. At $y=1$, the top boundary of this problem is set to describe the exact motion of the Mach 10 shock and it is given as follows

$$(\rho,u,v,p)(x,1,t)=\begin{cases}\left(8.0,8.25\cos\dfrac{\pi}{6},-8.25\sin\dfrac{\pi}{6},116.5\right), & x\in[0,s(t)),\\ (1.4,0.0,0.0,1.0), & x\in[s(t),4],\end{cases}$$

where $s(t)=\frac{1}{6}+\frac{1+20t}{\sqrt{3}}$. The simulations are performed on the computational domain discretized into $N_x\times N_y=2000\times 500$ uniform cells till $t=0.2$.

Fig. 25 plots the density contours, and it indicates that all considered schemes perform well in general. Again, careful inspection of Fig. 25 shows that WENO-IZ+$^{\rm A}$ and WENO-IZ+$^{\rm B}$ can reduce the numerical oscillations which are evidently observed in the results of WENO-Z+$^{\rm A}$ and WENO-Z+$^{\rm B}$, albeit not very thoroughly.

Remark 5.1. We can conclude that WENO-IZ+$^{\rm A}$ and WENO-IZ+$^{\rm B}$ outperform WENO-Z+$^{\rm A}$ and WENO-Z+$^{\rm B}$ respectively. Moreover, it can be seen that WENO-IZ+$^{\rm B}$ has indeed less dissipation and more resolution than WENO-IZ+$^{\rm A}$ in most tests (as shown in Table 1 and Figs. 5-7), and however, WENO-IZ+$^{\rm B}$ is also more oscillatory in some tests (see Fig. 23). Therefore, in the situations of flows with complicated fine smooth structures, WENO-IZ+$^{\rm B}$ should be recommended. On the other hand, in the situations of flows with shocks or strong discontinuities, WENO-IZ+$^{\rm A}$ should be recommended.

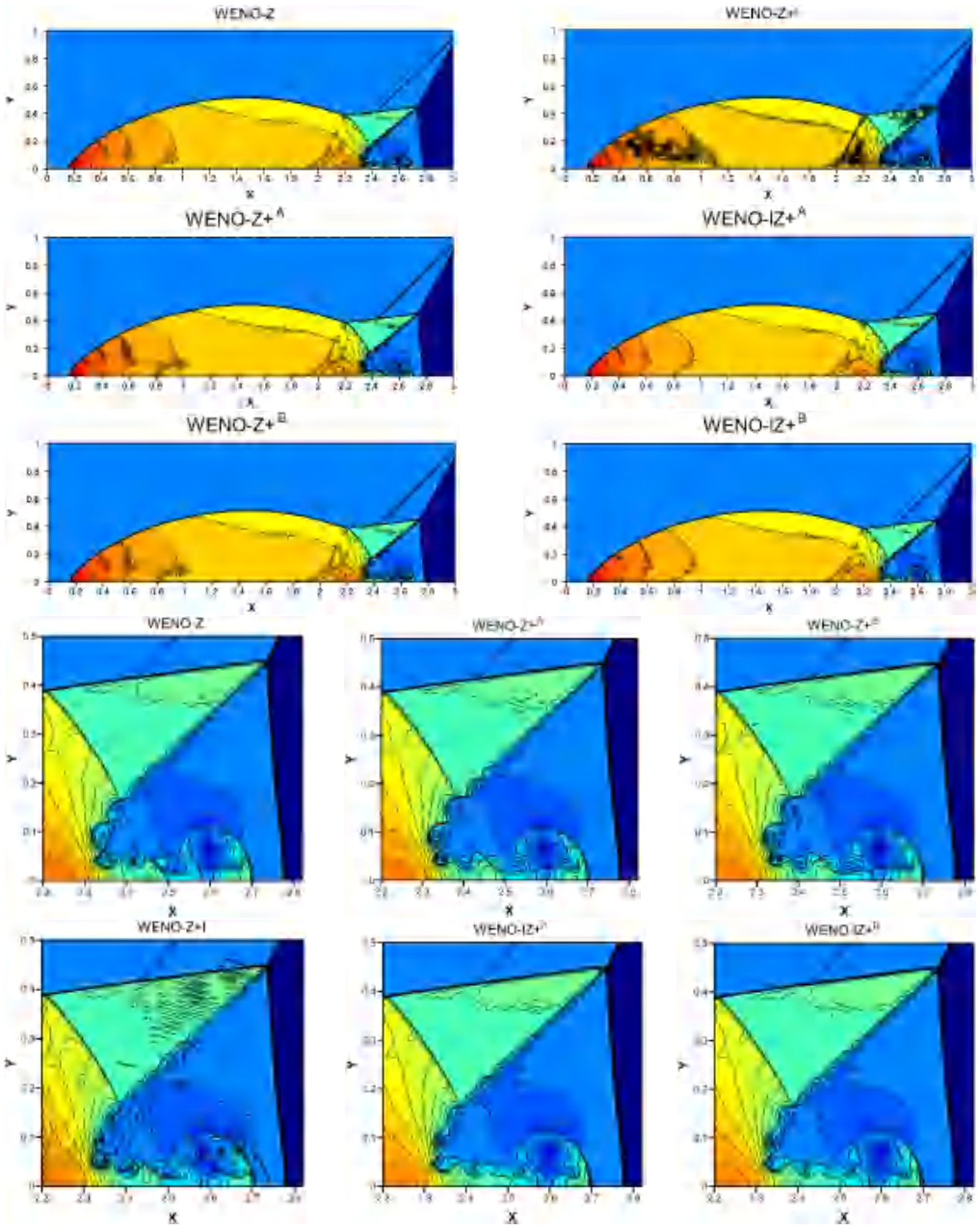

Figure 25: Numerical solutions of the DMR problem with $t=0.2$ and $N_x\times N_y=2000\times 500$.

6 Conclusions

This study has found that the over-amplifications of the nonlinear weights with respect to the nonsmooth or less-smooth substencils prevent the WENO-Z+ schemes from improv-

ing the resolution and preserving the stability. This is the crucial cause of the issue that the WENO-Z+ schemes have very low resolutions in solving 1D scalar advection problems containing high-order critical points with large output times and generate spurious oscillations on simulating problems with discontinuities or shocks, such as the Gaussian-square-triangle-ellipse linear test and the shock-tube problems. Inspired by this knowledge, we propose a method of modifying the additional term in the WENO-Z+ weights formula to avoid the over-amplifications of the nonlinear weights with respect to the nonsmooth or less-smooth substencils. The resultant scheme is named WENO-IZ+. Extensive numerical tests demonstrate that the performance of WENO-IZ+ is greatly improved in broad aspects. Firstly, the new schemes can successfully remove spurious oscillations in solving problems with discontinuities while maintaining good convergence properties in smooth regions. Secondly, they are able to achieve comparable or even better results than WENO-JS, WENO-Z, WENO-Z+ and WENO-Z+I at problems with high-frequency smooth waves like the shock-density wave interaction of Shu-Osher and Titarev-Toro. Thirdly, they can significantly improve the resolutions for long-run calculations of problems with discontinuities or high-order critical points. The performance of the WENO-IZ+ schemes on simulating 2D problems modeled via Euler equations has also been examined and it was illustrated that these proposed WENO schemes perform better than many other WENO schemes and they can eliminate or greatly decrease the post-shock oscillations.

Acknowledgements

The authors would like to thank the referees for the helpful suggestions.

References

[1] X. D. LIU, S. OSHER AND T. CHAN, *Weighted essentially non-oscillatory schemes,* J. Comput. Phys., 115 (1994), pp. 200–212.
[2] A. HARTEN, B. ENGQUIST, S. OSHER AND S. R. CHAKRAVARTHY, *Uniformly high order accurate essentially non-oscillatory schemes III,* J. Comput. Phys., 71 (1987), pp. 231–303.
[3] A. HARTEN AND S. OSHER, *Uniformly high order accurate essentially non-oscillatory schemes I,* SIAM J. Numer. Anal., 24 (1987), pp. 279–309.
[4] A. HARTEN, S. OSHER, B. ENGQUIST AND S. R. CHAKRAVARTHY, *Some results on uniformly high order accurate essentially non-oscillatory schemes,* Appl. Numer. Math., 2 (1986), pp. 347–377.
[5] A. HARTEN, *ENO schemes with subcell resolution,* J. Comput. Phys., 83 (1989), pp. 148–184.
[6] G. S. JIANG AND C. W. SHU, *Efficient implementation of weighted ENO schemes,* J. Comput. Phys., 126 (1996), pp. 202-228.
[7] A. K. HENRICK, T. D. ASLAM AND J. M. POWERS, *Mapped weighted essentially non-oscillatory schemes: Achieving optimal order near critical points,* J. Comput. Phys., 207 (2005), pp. 542–567.
[8] R. BORGES, M. CARMONA, B. COSTA AND W. S. DON, *An improved weighted essentially non-oscillatory scheme for hyperbolic conservation laws,* J. Comput. Phys., 227 (2008), pp. 3101–3211.

[9] F. ACKER, R. B. DE R. BORGES AND B. COSTA, *An improved WENO-Z scheme,* J. Comput. Phys., 313 (2016), pp. 726–753.
[10] X. LUO AND S. WU, *Improvement of the WENO-Z+ scheme,* Comput. Fluids, 218 (2021), 104855.
[11] R. LI AND W. ZHONG, *An extension of the order-preserving mapping to the WENO-Z-type schemes,* Adv. Appl. Math. Mech., 15 (2023), pp. 202–243.
[12] P. FAN, Y. SHEN, B. TIAN, AND C. YANG, *A new smoothness indicator for improving the weighted essentially non-oscillatory scheme,* J. Comput. Phys., 269 (2014), pp. 329–354.
[13] H. FENG, F. HU AND R. WANG, *A new mapped weighted essentially non-oscillatory scheme,* J. Sci. Comput., 51 (2012), pp. 449–473.
[14] H. FENG, C. HUANG AND R. WANG, *An improved mapped weighted essentially non-oscillatory scheme,* Appl. Math. Comput., 232 (2014), 453–468.
[15] R. LI AND W. ZHONG, *A robust and efficient component-wise WENO scheme for Euler equations,* Appl. Math. Comput., 438 (2023), 127583.
[16] R. LI AND W. ZHONG, *Locally order-preserving mapping for WENO methods,* J. Comput. Appl. Math., 424 (2023), 115004.
[17] S. CUI, Z. TAO AND J. ZHU, *A new fifth-order finite volume central WENO scheme for hyperbolic conservation laws on staggered meshes,* Adv. Appl. Math. Mech., 14 (2022), pp. 1059–1086.
[18] R. LI AND W. ZHONG, *A modified adaptive improved mapped WENO method,* Commun. Comput. Phys., 30 (2021), pp. 1545–1588.
[19] R. LI AND W. ZHONG, *An efficient mapped WENO scheme using approximate constant mapping,* Numer. Math. Theor. Meth. Appl., 15 (2022), pp. 1–41.
[20] R. LI AND W. ZHONG, *A new mapped WENO scheme using order-preserving mapping,* Commun. Comput. Phys., 31 (2022), pp. 548–592.
[21] R. LI AND W. ZHONG, *Towards building the OP-mapped WENO schemes: a general methodology,* Math. Comput. Appl., 26 (2021), 67.
[22] J. ZHU AND J. QIU, *New finite difference mapped WENO schemes with increasingly high order of accuracy,* Commun. Appl. Math. Comput., 5 (2021), pp. 64–96.
[23] R. LI AND W. ZHONG, *Improvement of the WENO-NIP scheme for hyperbolic conservation laws,* Axioms, 11 (2022), 190.
[24] R. LI AND W. ZHONG, *A general improvement in the WENO-Z-type schemes,* Commun. Comput. Phys., 31 (2022), pp. 1362–1401.
[25] R. LI AND W. ZHONG, *An improved component-wise WENO-NIP scheme for Euler system,* Mathematics, 10 (2022), 3881.
[26] F. ZENG, Y. SHEN AND S. LIU, *A perturbational weighted essentially non-oscillatory scheme,* Comput. Fluids, 172 (2018), pp. 196–208.
[27] C. W. SHU AND S. OSHER, *Efficient implementation of essentially non-oscillatory shock-capturing schemes II,* J. Comput. Phys., 83 (1989), pp. 32–78.
[28] V. A. TITAREV AND E. F. TORO, *Finite-volume WENO schemes for three-dimensional conservation laws,* J. Comput. Phys., 201 (2004), pp. 238–260.
[29] E. F. TORO AND V. A. TITAREV, *TVD fluxes for the high-order ADER schemes,* J. Sci. Comput., 24 (2005), pp. 285–309.
[30] V. A. TITAREV AND E. F. TORO, *WENO schemes based on upwind and centred TVD fluxes,* Comput. Fluids, 34 (2005), pp. 705–720.
[31] P. D. LAX, *Weak solutions of nonlinear hyperbolic equations and their numerical computation,* Commun. Pure Appl. Math., 7 (1954), pp. 159–193.
[32] E. F. TORO, Riemann Solvers and Numerical Methods for Fluid Dynamics-A Practical In-

troduction (Third Edition), Springer, 2009.
[33] J. QIU, B. C. KHOO AND C. W. SHU, *A numerical study for the performance of the Runge–Kutta discontinuous Galerkin method based on different numerical fluxes,* J. Comput. Phys., 212 (2006), pp. 540–565.
[34] C. W. SHU AND S. OSHER, *Efficient implementation of essentially non-oscillatory shock-capturing schemes,* J. Comput. Phys., 77 (1988), pp. 439–471.
[35] S. GOTTLIEB AND C. W. SHU, *Total variation diminishing Runge-Kutta schemes,* Math. Comput., 67 (1998), pp. 73–85.
[36] S. GOTTLIEB, C. W. SHU AND E. TADMOR, *Strong stability-preserving high-order time discretization methods,* SIAM Rev., 43 (2001), pp. 89–112.
[37] S. PIROZZOLI, *On the spectral properties of shock-capturing schemes,* J. Comput. Phys., 219 (2006), pp. 489–497.
[38] G. A. SOD, *A survey of several finite difference methods for systems of nonlinear hyperbolic conservation laws,* J. Comput. Phys., 27 (1978), pp. 1–31.
[39] P. WOODWARD AND P. COLELLA, *The numerical simulation of two-dimensional fluid flow with strong shocks,* J. Comput. Phys., 54 (1984), pp. 115–173.
[40] A. CHATTERJEE, *Shock wave deformation in shock-vortex interactions,* Shock Waves, 9 (1999), pp. 95–105.
[41] S. P. PAO, AND M. D. SALAS, A numerical study of two-dimensional shock-vortex interaction, AIAA 14th Fluid and Plasma Dynamics Conference, California, Palo Alto, 1981.
[42] Y. X. REN, M. LIU, AND H. ZHANG, *A characteristic-wise hybrid compact-WENO scheme for solving hyperbolic conservation laws,* J. Comput. Phys., 192 (2003), pp. 365–386.
[43] C. W. SCHULZ-RINNE, JAMES P. COLLINS, AND HARLAND M. GLAZ, *Numerical solution of the Riemann problem for two-dimensional gas dynamics,* SIAM J. Sci. Comput., 14 (1993), pp. 1394–1414.
[44] P. D. LAX AND X. D. LIU, *Solution of two-dimensional Riemann problems of gas dynamics by positive schemes,* SIAM J. Sci. Comput., 19 (1998), pp. 319–340.
[45] S. PIROZZOLI, *Numerical methods for high-speed flows,* Annu. Rev. Fluid Mech., 43 (2011), pp. 163–194.
[46] J. SHI, Y. T. ZHANG AND C. W. SHU, *Resolution of high order WENO schemes for complicated flow structures,* J. Comput. Phys., 186 (2003), pp. 690–696.
[47] Z. HONG, Z. YE AND X. MENG, *A mapping-function-free WENO-M scheme with low computational cost,* J. Comput. Phys., 405 (2020), 109145.
[48] R. ABEDIAN AND M. DEHGHAN, , *The formulation of finite difference RBFWENO schemes for hyperbolic conservation laws: an alternative technique,* Adv. Appl. Math. Mech., 15 (2023), pp. 1023–1055.
[49] R. LI AND W. ZHONG, *An improved fifth-order WENO scheme with symmetry-preserving smoothness indicators for hyperbolic conservation laws,* J. Comput. Phys., 491 (2023), 112350.
[50] C. ZHANG, Z. GAO, S. YE AND P. LI, *Edge detectors based on Pauta criterion with application to hybrid compact-WENO finite difference scheme,* Adv. Appl. Math. Mech., 15 (2023), pp. 1379–1406.
[51] Y. ZHANG AND J. ZHU, *New finite volume mapped unequal-sized WENO scheme for hyperbolic conservation laws,* Adv. Appl. Math. Mech., 16 (2024), pp. 459–492.